Universidad Nacional Autónoma de México

Facultad de Ciencias

Photodetachment experiments on As^-, Au^- and Ag^-.

Experimental procedure to measure cross sections and electron affinities.

T E S I S

que para obtener el título de:

Física

P R E S E N T A :

Denisse Cruz Pérez

TUTOR

Dr. remigio cabrera trujillo
Instituto de Ciencias Físicas, UNAM

Ciudad Universitaria, CDMX, 2021

Contents

Figures

Tables

Acronyms & Abbreviations

ACB	Animated Crossed Beams technique
AMS	Atomic Mass Spectroscopy
CEM	Channel Electron Multiplier
EA	Electron Affinity
ECR	Electron Cyclotron Resonance
FC	Faraday Cup
GUNILLA	Gothenburg University Negative Ion Laser LAboratory
IR	Infrared
LPT	Laser Photodetachment Threshold
MOPO	Master Optical Parametric Oscillator
NAPS	NAnoscopic PhysicS group
Nd-YAG	Neodymium-doped Yttrium Aluminum Garnet
OPA	Optical Parametric Amplifier
OPO	Optical Parametric Oscillator
TOF	Time Of Flight
Ti:Sa	Titanium-Sapphire lasers
UV	Ultraviolet
UCL	Université Catholique de Louvain

Abstract

Negative ions are of fundamental importance in nature ranging from the Sun's absorption spectra to their use in tokamak fusion reactors. Laser Photodetachment Threshold spectroscopy (LPT) and Animated Crossed Beams (ACB) are experimental techniques used to study negative ions. The research presented in this thesis has been performed at the Gothenburg University Negative Ion Laser LAboratory (GUNILLA), in Sweden, and at the Nanoscopic PhysicS group (NAPS) of the Université Catholique de Louvain, in Belgium.

I report experimentally measured absolute photodetachment cross sections of Ag^- and Au^-. Measurements of the absolute photodetachment cross section of Au^- and Ag^- were performed at NAPS by means of ACB. Furthermore, measurements on the electron affinity (EA) of As^- and Au^- were performed at GUNILLA.

Finally, the pulsing mode of the ion source was implemented to investigate the cathode lifetime extension. Here, gold was used, in which the results show a positive outcome. In addition, the EA of Au^- is being reported.

Our final results show that measuring the photodetachment of negative ions is possible for an undergraduate student when advanced experimental accelerators are available.

keywords: Atomic Physics, Photodetachment, Negative Ions, Laser Photodetachment Threshold, Animated Crossed Beams.

Chapter 1

Introduction

Negative ions are atomic systems with a net negative charge [1]. It could be easy to consider negative ions similar as positive ions. The formation of the latter requires to supply the necessary energy to remove one or more electrons from the atomic shell, while for the negative ions, a neutral atom should attach to an electron. One of the interesting properties of negative ions is that there is no long range attraction [2] between the extra electron and the atom. Nevertheless, negative ions exist due to the so called electron correlation. This represents a fruitful research field in atomic physics.

The development of the theories of the atomic structure, mainly through the 20th century, led to the study of negative ions. J.J. Thomson [3] was the first to observe negative ions in gas phase. In 1953 Wildt prompted the first experimental study of photodetachment of H^- [4] and later his group measured the electron affinity of oxygen via photodetachment, using standard lamps.

The role of negative ions is fundamental in the atomic theory due to the large importance of electron interactions. Given the extra electron in this type of atomic system, a repulsive interaction is produced between the atom electron cloud and the extra electron. Therefore, they are quantum systems where the electron correlation plays a major role [5].

In spite the importance of describing electron correlation effects, it is theoretically difficult to describe negative ions. In order to know more about these systems, it is of importance to study their properties. One of them is the electron affinity (EA) that is defined as the binding energy of an extra electron. The EA explains the fundamental quantum characteristics of atoms. Negative ions can be studied using the photodetachment process, where a negative ion absorbs a photon and breaks up in a neutral atom and a free electron. The onset of this process is described by Wigner's threshold law [6].

The objectives of the experiments with photodetachment are to obtain EA values not measured before, updating the values for the EA obtained in the past, and measuring the widths of states and the energies of the resonant states of the elements. The negative ions provide us key features to analyze the structure and also the dynamics of many-electron systems [7].

There is wide a variety of negative ions. For example, in the thermonuclear fusion field in Tokamak reactors a beam of D^- is accelerated, then the extra electron is removed. The resulting neutral D is then used to heat the plasma. Here the photodetachment technique is implemented for a more successful outcome [7]. One of the important applications is in Atomic Mass Spectrometry (AMS) [8], which is the most susceptible method for trace element analysis. It is based on a tandem accelerator, where the negative ion beam is converted into positive ones at the high voltage terminal. Interfering isobars can here be removed prior to injection into the accelerator using the photodetachment process [7, 8]. Negative ions are meaningful not only for their importance in various applications, but also for the purpose of understanding their atomic properties. Furthermore, they play an important role in chemistry when studying chemical molecular interactions, as well as in the field of astronomy when studying the interstellar media.

In the experimental part, the production of negative ions is performed in a sputtering source. The negative ions then created are further accelerated with electrostatic fields into an interaction region, where they are exposed to laser light in either perpendicular, parallel or antiparallel configuration. The extra electron can be detached from the negative ion provided that the photon energy is sufficiently large. Lasers detach the extra electron from the anions, in which the wavelength of the electromagnetic radiation depends on the element or molecule under study. After seven years of creating the first laser by Theodore H. Maiman at Hughes Research Laboratories in 1960 [9], the application of lasers for photodetachment experiments was made possible by Brehm *et al.* [10] when determining the EA of He^-. Nowadays, the EA of most of the stable elements of the periodic table has been determined. The laser is a very important tool in many areas of physics and it is possible to use different laser types to perform spectroscopic studies. When it was found that lasers could be applied in atomic physics studies, they were limited to generate a fixed wavelength. With the further development of laser technology, they evolved from only producing a certain wavelength, to a range of wavelengths that cover the spectral range from the far infrared (IR) to the ultraviolet (UV) regions [11]. Using narrow bandwidth lasers allowed high precision measurements.

Beside the above characteristics for laser, photodetachment studies require a well-characterized sample of negative ions, a sufficiently intense beam, and a suitable detector for the reaction products [12]. It is possible to find those characteristics at the following facilities: Gothenburg University Negative Ion Laser LAboratory (GUNILLA) [13], in Sweden, and at the Nanoscopic PhysicS laboratory of the Université Catholique de Louvain (UCL), in Belgium, where the experimental work took place and it can be described

as follows.

Silver and gold are two of the most known heavy metals, while arsenic must be carefully manipulated [14]. In the aim of deepening in the knowledge of these elements measurements on As^- and Au^- where done by applying the Laser Photodetachment Threshold spectroscopy (LPT) for EA measurements and improvement, where a pulsed ion source was used on the latter to investigate a gold cathode lifetime improvement. Animated Crossed Beams technique (ACB) [15] was applied to measure absolute cross sections of Ag^- and Au^-. This experimental technique was compared to the LPT and was the motivation for these studies. LTP spectroscopy allowed to scan the wavelength of the laser light on a parallel alignment, while ACB allowed to intersect the negative ion beam with a laser beam in a perpendicular geometry.

The work presented here aimed at measuring two different properties through the use of two different instruments using complementary techniques of photodetachment. Both, have pros and cons in their construction and performance. This thesis focus on the EA measurements on As^- and Au^- using both the continuous and pulsed modes of the ion source at GUNILLA, while at NAPS cross sections of Ag^- and Au^- were obtained.

The results presented here aim to contribute to the understanding of the atomic structure of the above mentioned elements, focusing on the following questions:

- Could the accuracy of the determination of the EA of As^- be improved?
- Is it possible to extend a gold cathode lifetime with a pulsed ion source and measure its EA?

Chapter 2

Basic Properties of Negative Ions: Theory

At the beginning of the last century, the new ideas of Louis de Broglie, Erwin Schrödinger, Niels Bohr, and Werner Heisenberg, at the birth of modern physics, opened a different path to study matter through the novel theory of quantum mechanics. Bohr's contribution to the description of the H atom [16] and the de Broglie's wave-particle theory [17], provided the basis for the description of matter that had never been seen before with classical mechanics. The main idea was the dual behavior of a particle as a wave characterized by a wavelength λ, which is related to its momentum p through h, Planck's constant, in the following way:

$$\lambda = \frac{h}{p}. \tag{2.1}$$

This, de Broglie equation relates wavelength and momentum that all particles exhibit. Heisenberg continued the work by postulating the uncertainty principle, specifying that the position and momentum of a particle could not be exactly calculated [18], as consequence of the uncertainty relation

$$\Delta x \Delta p \geq \frac{h}{4\pi}. \tag{2.2}$$

Heisenberg's principle stipulates that the position and momentum of a particle can not be determined at the same time with better accuracy than Planck's constant divided by

4π. Heisenberg's principle of uncertainty is a consequence of the wave nature of particles in the quantum sense. The introduction of the wave function as a path to solve Schrödinger equation allows to predict and derive these properties.

2.1. Single electron models

The particle in a square box is the first model in a quantum physics course. It is a good illustration for bound states of a single electron, its wave functions, and eigenenergies [2]. Using the Schrödinger equation of a single particle, we can obtain the solutions for the electron in the box

$$H\Psi_n(x,t) = \left[\frac{\hbar^2}{2m}\nabla^2 + V(x,t)\right]\Psi_n(x,t) = i\hbar\frac{\partial}{\partial t}\Psi_n(x,t), \tag{2.3}$$

where H is the Hamiltonian operator. The time derivative of the right hand side is equal to E_n, the quantized eigenenergy, for the case of a stationary solution.

Another example of single electron models is the Hamiltonian for a central potential

$$H = -\frac{\hbar^2}{2m_e}\nabla^2 + V(r), \tag{2.4}$$

where *V(r)* is the radial potential given by the Coulomb interaction,

$$V(r) = -\frac{Ze^2}{4\pi\epsilon_0 r}. \tag{2.5}$$

Here e is the elementary change, ϵ_0 is the vacuum electric susceptibility, and Z is the atomic number.

The Schrödinger equation for the Hamiltonian in Eq. (2.4) can be solved with wave functions in a spherical coordinate system with separable parts

$$\Psi(r,\Omega,s) = R_{n,l}(r)Y_{l,m_l}(\Omega)\xi_{m_s}(s). \tag{2.6}$$

Here, $R_{n,l}$ is the radial function that depends on the radial coordinate, Y_{l,m_l} is the spherical harmonic function that describes the angular dependence, and ξ_{m_s} is the spin [2]. The Schrödinger equation has solutions that correspond to the eigenenergies

$$E_n = -\frac{Z^2 m e^4}{2\hbar^2 n^2 (4\pi\epsilon_0)^2}. \tag{2.7}$$

Herewith, we can see there are discrete energy levels in an atom, and that when an electron is excited with a laser it can be removed from the energy level it is placed in.

2.2. Negative Ions

In an atom the outermost electron feels a long range attractive Coulomb force, in which the Coulomb potential decreases as $1/r$, where r is the distance between the electrons and the center of the nucleus. The existence of negative ions is possible despite the fact that, in a neutral atom, an electron is not affected by a long range attraction [2]. However, when the electron moves closer to the nucleus, it polarizes the electron cloud. Furthermore, electron correlation also occurs in atoms, but then the Coulomb attraction between the electron and the nucleus dominates, making it difficult to model the electron correlation. Therefore, negative ions are good systems to test electron correlation calculations since it is a dominating force and their study can teach us more about the properties of atomic systems. One of these properties is the EA which is defined as the difference in the total energy (E_{tot}) between the ground state of the neutral atom (A) and the ground state of the corresponding negative ion (A^-)

$$EA(A) = E_{tot}(A) - E_{tot}(A^-). \tag{2.8}$$

We can see a representation of the EA in Fig. 2.1 and from Eq. (2.8), we can say that having a stable negative ion means having a positive EA.

It is also important to mention that almost all the elements have a stable EA, although that is not the case for the noble gases, nitrogen, magnesium, and a few more elements. Theoretical calculations predict the EA of elements, nevertheless, the most accurate values for the EA have been obtained experimentally [7].

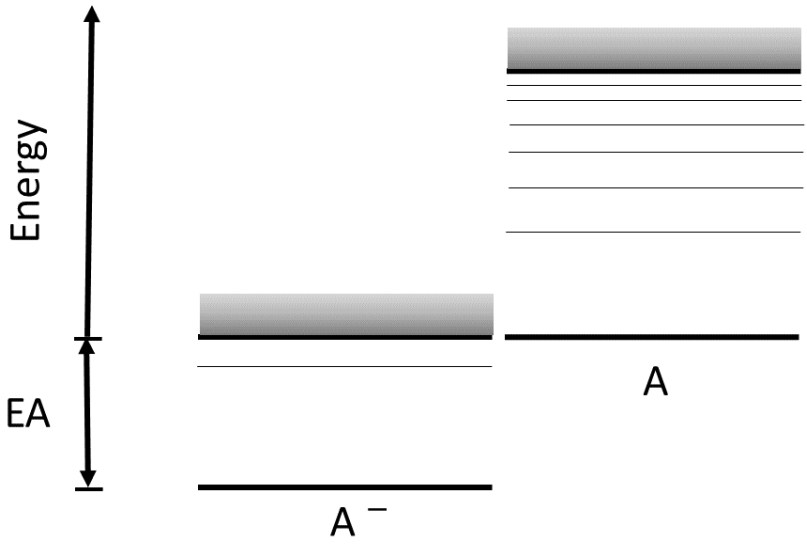

Figure 2.1: Scheme of the energy levels in the negative ion A^- and the ground state A.

2.3. Photodetachment

Light is responsible for many of the processes in nature. In the quantum picture we consider light as a single energy photon γ, with energy $E = h\nu$, where ν is the photon frequency and h is Planck constant. We call photodetachment the interaction of electromagnetic radiation with a negative ion that causes the release of an electron and leaves a neutral atom or molecule behind.

The photodetachment process can be described as follows:

$$A^- + \gamma \longrightarrow A + e^-. \tag{2.9}$$

From Eq. (2.9) we can see that a photon (γ) is absorbed by a negative ion (A^-) resulting in the removal of an electron [2].

From energy conservation the photodetachment process only can occur if the photon has more energy than the EA of the negative ion. The remaining photon energy is carried away by the electron as kinetic energy. Fortunately, for most photodetachment experiments the small binding energies involved permits the use of light which easily can

be produced with commercially available lasers.

The laser photon energy required for the outermost electron to be ejected is determined by the binding energy of the negative ion. Consequently, photodetachment can be used to measure the EA of an atom by making a scan with a varying frequency laser to determine the threshold energy. When the electron is released from the atom, it will feel a weak interaction that can be approximated by the centrifugal and polarization terms. These terms are described as [19]

$$V_{eff}(r) = \frac{l(l+1)}{2r^2} - \frac{\alpha}{2r^4}, \tag{2.10}$$

where the distance from the emitted electron and the atomic core is r, l is the angular momentum of the emitted electron and α is the dipole polarizability of the neutral atom. The dipole interaction goes as $1/r^4$, i.e. that for long distances it decays faster than $1/r$. A normal atom decays as $1/r$ because it is attracting the electrons [20]. Then, the long range interaction from valence electrons does not exists given the fast decay.

2.4. The Wigner Threshold Law

In Laser Photodetachment Threshold spectroscopy (LPT), the photon energy is varied over the threshold region for photodetachment. The yield of photodetachment signal as a function of photon energy is used to fit Wigner's Law [20].

Eugene Paul Wigner was a theoretician who among all his work, made contributions in the photodetachment theory. He realized that at small energies above threshold, the centrifugal term dominates the effective potential . Using this assumption, he derived an analytical expression for the shape of the cross section near threshold energy, in it, he relates the cross section with the interaction potentials. In the case of photodetachment the short range polarization potential leads to Wigner's law [6]

$$\sigma = C(E - EA)^{l+\frac{1}{2}}, \tag{2.11}$$

where C is a scaling constant, E is the photon energy ($h\nu$), the threshold energy equals the EA of the neutral atom, and likewise the minimum energy required to release the additional electron, it marks the beginning of the rise in the cross section [21]. Here, l is the orbital angular momentum of the ejected electron [22] and $\frac{1}{2}$ originates from the density of states in the continuum (scattering states) [2, 23].

Given the effective potential in Eq. (2.10), the determination of the EA of the elements is carried out by measuring the photon energy threshold of the transition. This occurs from the negative ion ground state to the neutral atom ground state. Sometimes, it is favorable to measure the onset due to the formation of an excited state A* of the neutral and subtract the normally accurately known excited state energy of A* [12]. Based in Eq. (2.11), with $l = 0$ we have a s-wave threshold which means $m = 0$ and there is not an orbital splitting. With $l = 1$ we have a p-wave, where there is splitting of orbitals into triplets, with $m = -1, 0, +1$, a representation of this behavior can be seen in Fig. 2.2.

Cross sections for photodetachment are zero at threshold and they describe the probability for a process to occur at above threshold energies. The threshold behavior for systems without the Coulomb interaction is determined by the dynamics of the residual atom and the emitted electron [7]. Cross section and EA are features that describe the electron configuration of atomic systems.

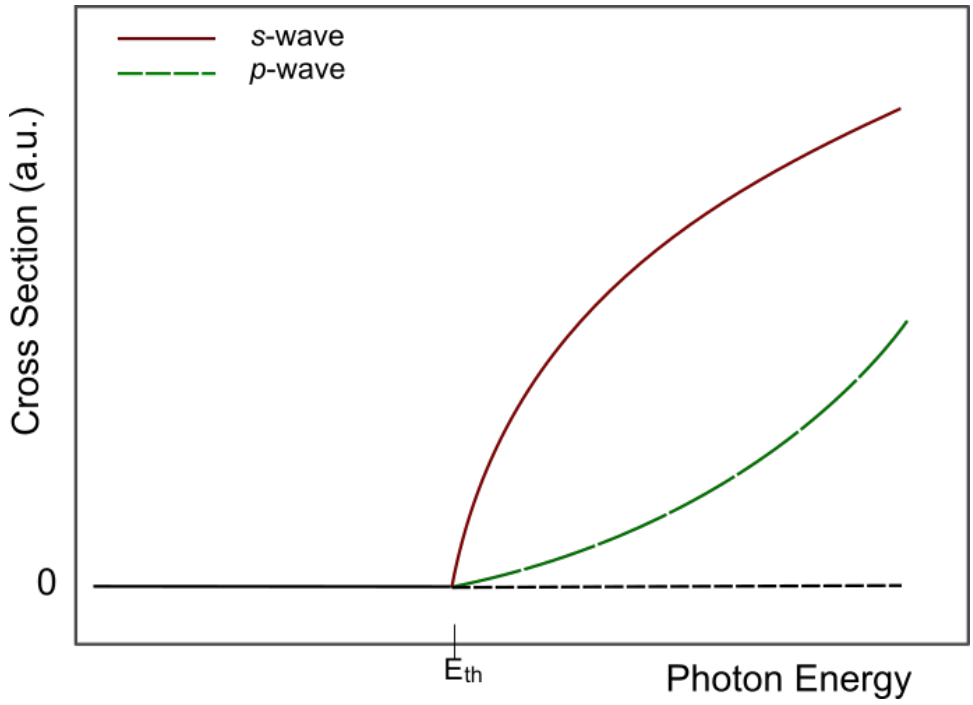

Figure 2.2: Behavior of the detached electron described by Wigner's threshold law. s-wave (solid line) with $l = 0$ and p-wave (long dashed line) with $l \geq 1$.

2.5. On the origin of Wigner's threshold law for photodetachment

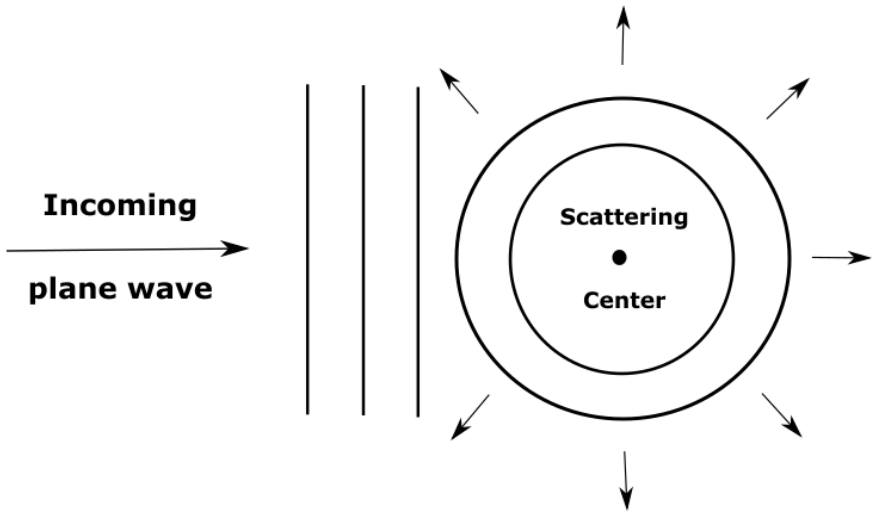

Figure 2.3: Scattering geometry: An incoming plane wave from the left is scattered from a scatterer. The scattered part of the wave is an angularly modulated spherical wave (2.12). For clarity the outgoing plane wave is omitted.

Inelastic scattering induces a transition from the initial state of the target particle, here a negative ion, to a different final state [24]. The normalised asymptotic wave function is

$$\psi(\mathbf{r}) = \delta_{ji} e^{ik_i \cdot z} + \frac{e^{i\mathbf{k}_j \cdot \mathbf{r}}}{r} f_{j,i}(\Omega), \tag{2.12}$$

valid for $r \to \infty$. Here $k_j = \sqrt{\frac{2\mu(E-E_j)}{\hbar^2}}$ is the asymptotic wavenumber of the outgoing electron in the open channel j and μ is the reduced mass of the electron (see Fig. 2.3). The first term in Eq. (2.12) is the incoming plane wave along the z-axis that represents the incoming particle current (incident photon), and the second term is the outgoing angularly modulated spherical wave (photodetached electron). Most of the plane wave passes the scattering centre forming the so called forward scattered part. The angular modulation $f_{j,i}(\Omega)$ of the spherical wave contains most of the information concerning processes at the scattering centre and known as the scattering amplitude. Most prominently, the outgoing particle current through a specific solid angle is proportional to $f_{j,i}(\Omega)$ such that the inelastic differential cross section becomes

$$\frac{d\sigma_{i,j}}{d\Omega} = \frac{outgoing\, flux}{incoming\, flux/area} = \frac{k_j}{k_i} |f_{j,i}(\Omega)|^2 \tag{2.13}$$

The scattering amplitude $f_{j,i}(\Omega)$, in the first Born approximation, is essentially the matrix element for the transition between the final state and the incoming plane wave,

$$f_{j,i}(\Omega) = -\frac{\mu}{2\pi\hbar^2}\sum_n \int e^{-i\mathbf{k}_j\cdot\mathbf{r}'} V_{j,n}\psi_n(\mathbf{r}')d\mathbf{r}'. \tag{2.14}$$

Here the potential $V_{j,n}$ determines the Ω dependence of $f_{j,i}(\Omega)$. To further clarify this point we expand the plane wave and the final state in spherical harmonics. Inserting this in Eq. (2.14) and using the orthogonality of the spherical harmonics we obtain

$$f_{j,i}(\Omega) = -\frac{\mu}{2\pi\hbar^2}\sum_n \int \left[4\pi\sum_{l=0}^{\infty}\sum_{m=-l}^{l}(-i)^l j_l(\mathbf{k}_j\cdot\mathbf{r}')(-1)^{-m}Y_{l,m}(\Omega_{k_j}))\right] V_{j,n}(r)\alpha_{n,l'}\delta_{ll'}\delta_{mm'}dr. \tag{2.15}$$

Here in $j_l(x)$ is a spherical Bessel function, $Y_{l,m}$ a spherical harmonic, and $\alpha_{n,l',m'}$ are the expansion coefficients of the final state. In the vicinity of the threshold, k_j is small and the Bessel function $j_l(\mathbf{k}_j\cdot\mathbf{r}')$ can be approximated as k_j^l [25]. Close to the threshold, all other terms in Eq. (2.15) can be considered as constant. To obtain the integrated cross section for inelastic scattering we have to square $f_{j,i}(\Omega)$ and multiply by k_j/k_i. This leads to Wigner's law for cross sections $\sigma_{ij}(E) \approx Ck_j^{2l+1} \approx C(k_j^2)^{l+1/2}$ at the threshold of inelastic scattering channels. Since $k_j^2 = 2\mu(E - EA)$ with E the initial photon energy and EA the bound electron affinity, then

$$\sigma_{ij}(E) \approx C(E - EA)^{l+\frac{1}{2}}. \tag{2.16}$$

Close to photodetachment thresholds usually only the cases $l = 0$, 1, also called s-wave and p-wave, for the ejected electron, are important. The s-wave has an onset with an infinite slope which facilitates a precise determination of the threshold position. All higher orbital angular momenta lead to thresholds with zero slope at the threshold. The sharp onset of the s-wave detachment cross section is a remarkable feature, and one can question how sharp it can become.

2.6. As^-, Au^- and Ag^- ions

The systems under study, in this work, are the As^-, Au^- and Ag^- ions. Their electron configuration is described as follows:

Arsenic

Arsenic has the atomic number 33 and forms a number of poisonous compounds. It is widely distributed throughout the Earth's crust and can be released into the atmosphere and water through natural and human activities [14].

The ground state of As$^-$ is $4p^4\ ^3P_2$ and the ground state of As is $4p^3\ ^4S_{3/2}$. The binding energies for the three fine structure components in the negative ion are: for $J = 2$ is 0.8048(2) eV, for $J = 1$ is 0.6772(2) eV, and for $J = 0$ is 0.6405(10) eV, and the photodetachment is an s-wave transition [22]. These values correspond to wavelengths of 1541 nm, 1831 nm and 1935 nm, respectively, for the photodetachment thresholds. A diagram of the energy levels is shown in Figure 2.4.

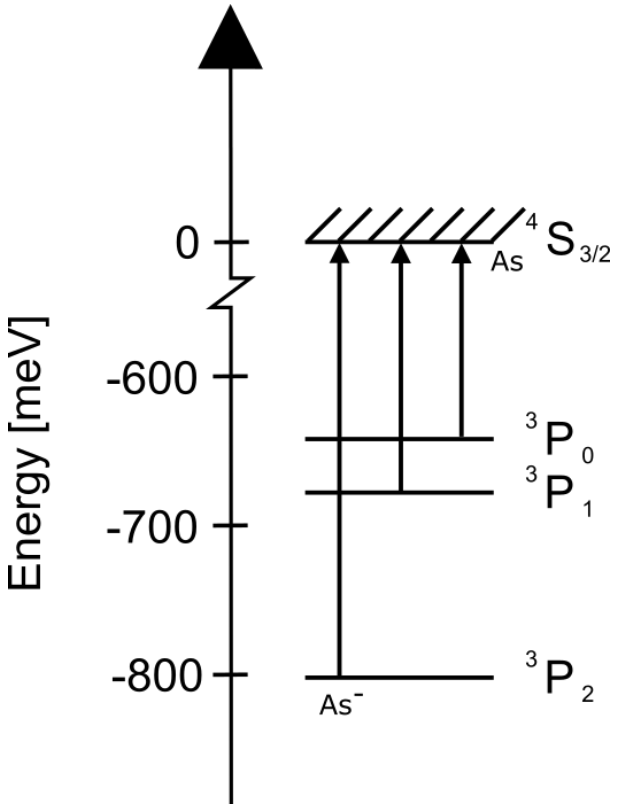

Figure 2.4: Energy level diagram of As$^-$ and As [22].

Gold

Gold has the atomic number 79. It is one of the least reactive elements and it is in the same group as Ag. The absolute photodetachment cross section for gold is known experimentally to be $\sigma_{Au} = (2.6\pm30\,\%)\times10^{-18}$ cm^2 at 2.37058 eV (523 nm) that corresponds to 19120.017 cm^{-1} [26].

The ground state of Au$^-$ is $5d^{10}\ 6s^2\ ^1S_0$ and the ground state of Au is $5d^{10}\ 6s\ ^3S_{1/2}$. Its EA is 2.3086 eV and the photodetachment is a p-wave transition. This value corresponds to a wavelength of 537.329 nm for the photodetachment threshold [26]. Au was used at

NAPS to improve the photodetachment cross section value. A diagram with the ground state energy levels of Au^- and Au is shown in Figure 2.5.

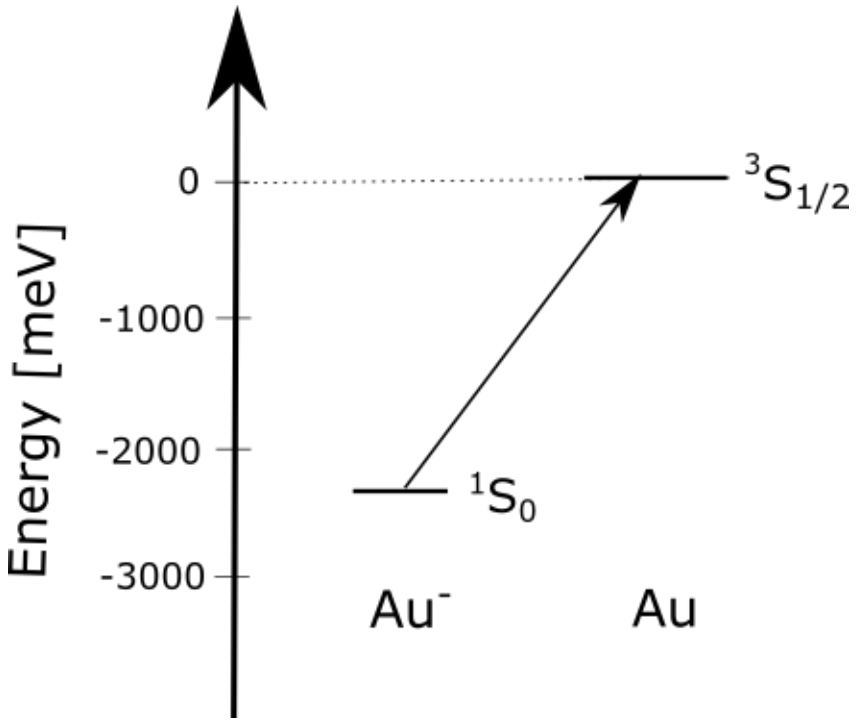

Figure 2.5: Energy level diagram of Au^- and Au [26].

Silver

Silver has the atomic number 47. The metal is found in the Earth's crust in the pure form. The ground state of Ag^- is $4d^{10}5s^2\ ^1S_0$ and the ground state of Ag is $4d^{10}5s\ ^2S_{\frac{1}{2}}$. Its EA is 1.304 eV and the photodetachment is a p-wave transition, according to [27]. This value corresponds to a wavelength of 951.232 nm for the photodetachment threshold. A diagram with the ground state energy levels of Ag^- and Ag is shown in Fig. 2.6.

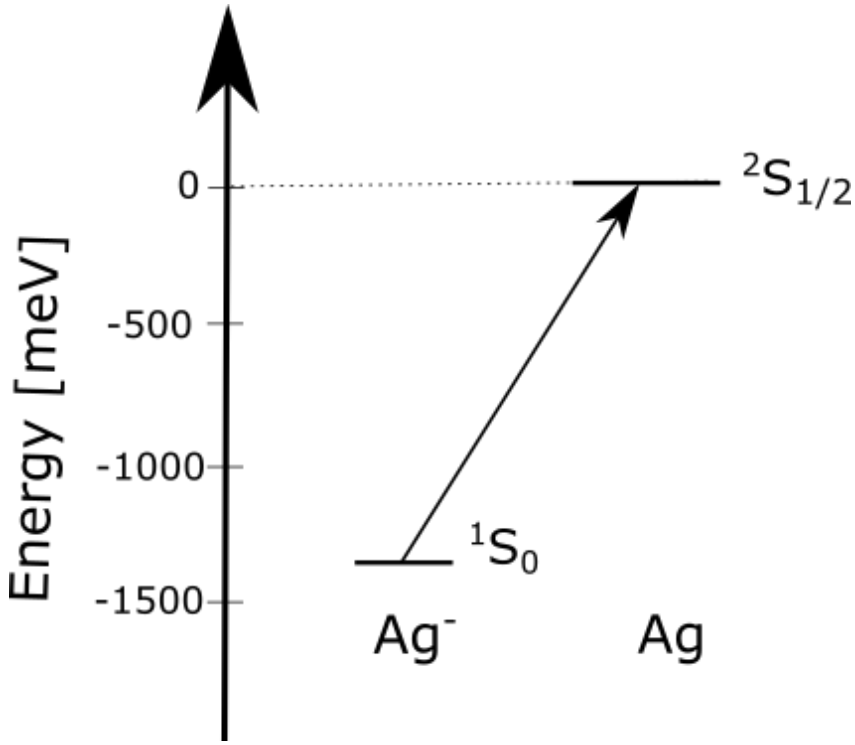

Figure 2.6: Energy level diagram of Ag^- and Ag [27].

Chapter 3

Experimental Method

The experiments in this thesis were performed at the University of Gothenburg, Sweden and at the Catholic University of Louvain, Belgium. In both facilities a beam of stable negative ions were produced which were then allowed to interact with a laser beam.

The experiment applies the LPT method, where the production of negative ions starts with a negative sputter ion source that is connected to a system of ion beam optics used to guide the negative ion beam to a magnet, which selects the masses of interest, through their kinetic energy, their momentum and trajectory. Afterwards, there is an interaction region where negative ions and photons interact, resulting in an encounter that is detected by the neutral particle detectors and recorded for later data analysis. The experiment needs to be conducted at vacuum. To have conditions to achieve the free path that is sufficiently long to allow the ion beam to be transported through the apparatus, a vacuum lower than 10^{-6} mbar is required. The negative ion beam can be neutralized by collisions of the residual gas and the goal is to have a sufficiently long mean free path of the negative ion beam. The result of the collisional background is noise for the signal events.

In order to increase and thus maximize the interaction between ions and photons it is of advantage to have a parallel or antiparallel alignment. When the ion and the laser beams are in one of these geometries there would be a Doppler shift in the frequency which has to be taken into account. This is because an ion in motion will observe an effective photon frequency which differs from the laboratory photon frequency [5]. The count rate depends on the laser beam and ion beam overlap, so it is essential to maintain the same overlap during a complete threshold scan. The laser frequency measured in laboratory ω_0 differs from the effective frequency ω_e observed by the ions due the ion velocity v and the angle θ between the laser and ion beam given by the geometry of the

experiment. The following formula describes the Doppler effect frequency [5]:

$$\omega_0 = \omega_e \frac{1 + \frac{v}{c}\cos\theta}{\sqrt{1 - \frac{v^2}{c^2}}}. \tag{3.1}$$

Here, the Doppler effect is discriminated and as a result, experiments with a perpendicular geometry avoid frequency changes due to the Doppler effect. Nevertheles, the experiments performed at GUNILLA had a parallel and antiparallel geometry ($\theta = 0°, 180°$), respectively. These geometries allow to define a larger interaction region in comparison with other geometries, where ω_0 is the laser frequency, v is the velocity of the ions, θ is the angle between the laser and ion beam, and c is the speed of light [28]. Knowing that $E = \omega\hbar$, two cases could be derived and for low kinetic ion energies of KeV, where $v \ll c$ holds, the non-relativistic Doppler shift [21]:

$$E_{(p)} = E\left[1 \pm \frac{v}{c}\right]. \tag{3.2}$$

For the Au experiment, Eq. (3.2) in the propagative form (+) was used to calculate the Doppler shift given that the experiment was performed in a parallel geometry, and for the As experiment, the antiparallel relation (-) was used. Once having the Dopppler shifted value $E_{p,a}$, the error propagation comes as the difference between two different values of $E_{p,a}$ which are dependent of two different voltages: V and $V - \delta V$ from the ion source. At GUNILLA the error propagation is given by

$$\Delta E_{p,a} = |E_{p,a}(\theta, V) - E_{p,a}(\theta, V - \delta V)|. \tag{3.3}$$

Therefore the Doppler shifted value is given as $E_{p,a(\theta)} \pm \Delta E_{p,a(\theta)}$, where $V = 6\ KeV$ and $V + \delta V = 5.9\ KeV$.

3.1. System Parts

3.1.1. Sputter Ion Sources

Cesium sputter sources have been used since V.E. Khrohn in 1962 [29] discovered that yields of negative ions can be improved in the presence of cesium. Middleton provided recipes and the suitable conditions to produce a specific negative ion in *"The Negative Ion*

Cookbook" [30]. The sputter sources used in the experiments at GUNILLA is a Middleton type, whereas the source at NAPS is home built.

In the sputter ion source, there is a cesium reservoir, where cesium is heated up, then evaporates and is sprayed via a tube onto a helical or spherical ionizer. The cesium cloud is then ionized and the atoms are accelerated towards the cathode by an electric potential of a few kV.

The cathode is a cylinder usually made of aluminium or copper with a hole in which the element of interest can be placed. In order to provide conductance, a mix of the element and a conducting material can be made [20]. When the cesium atoms hit the ionizer they will sputter the cathode surface and they will form a cesium layer on top of the cathode. Atoms sputtered out from the cathode can then capture an extra electron from the cesium atoms making them negative. The negative ions formed in this process are accelerated towards the hole in the Cs ionizer. The negative ion beam is then extracted from the ionizer and then further accelerated.

3.1.2. Mass Selecting Magnet

The negative ion beam contains different atoms and molecules that are accelerated to the same kinetic energy, but since the interest constrains onto a specific element, it is necessary to isolate it from the rest. This is possible by making use of a mass selecting magnet that selects certain elements with a specific mass. Particles with different momenta will follow a divergent path. This makes possible the use of a dipole magnet as a mass spectrometer. The focusing of the magnet could be in one or two dimensions depending of the construction of the magnet, in which slits and apertures are needed. At GUNILLA, the primary ion beam (green arrow Fig. 3.1) enters to the one direction slit magnet and feels a vertical magnetic field where the Lorentz force points towards the center [31]. The magnetic field strength is arranged depending on the element or isotope of interest. The mass over charge ratio $\frac{m}{q}$ of one favored ion species is transmitted successfully through object and image slit before and after the magnet [21]. Meanwhile, heavier ions will not be deflected enough and the trajectory of lighter ions will be bent more than necessary to reach the image slit [28].

The second slit cuts the passage of the masses with a different trajectory from the central one. This is given by the equilibrium of the centripetal and Lorentz forces [20]

$$\frac{mv^2}{\rho} = qvB, \tag{3.4}$$

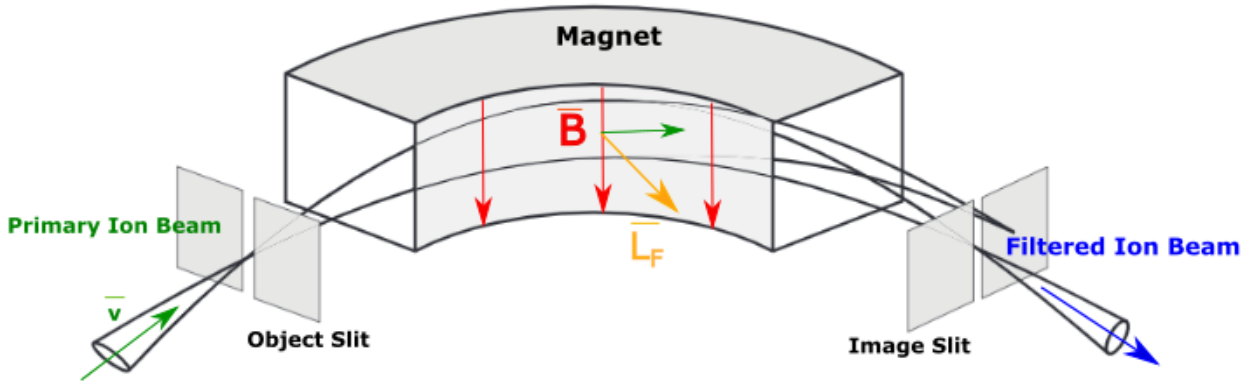

Figure 3.1: Single-focusing 90° dipole bending magnet with a bending radius of 500 mm [13]. The primary ion beam enters to the object slit and feels a magnetic field. The mass of interest will follow the central path, while different masses will follow other paths and therefore miss the image slit to the image point where the filtered ion beam emerges [20].

where ρ is the radius of the central trajectory inside the magnet and B is the magnetic field. The filtered ion beam follows the path towards the focusing optics to the interaction region.

3.1.3. Lasers

The first laser was built in 1960 by Theodore H. Maiman at Hughes Research Laboratories. It differs from other light sources because it emits coherent light [32]. To perform laser photodetachment threshold experiments, lasers are needed where the wavelength can be varied. This can be done with a fixed frequency laser pumping a tunable laser system. For this work Nd-YAG, Ti:Sapphire and diode lasers were used to obtain different photon enegies and a tunable radiation over a wide energy range. A Nd-YAG laser was used to pump an Optical Parametric Oscillator (OPO) and Optical Parametric Amplifier (OPA). The key operation process for OPO is quite different from other laser systems. While other lasers acquire spontaneous and stimulated emission generated by atomic transitions, the OPO system acquires emission by a nonlinear frequency conversion process [33]. The optical parametric process eliminates one photon and create two new photons. From those two, one has a higher energy which is called the signal and the other has a lower energy and is called the idler [20]. This process conserves the energy as

$$E_{pump} = E_{signal} + E_{idler}. \tag{3.5}$$

Once a strong down-converted beam is establish from the OPO, this can follow a subsequent optical parametric for amplification which as its name says, amplifies the beam. This part is the so called OPA [20].

On the other hand, Ti:Sapphire (Ti:Sa) lasers are built in similar ways as other types of solid-state lasers. A Ti:Sa crystal is placed between two curved mirrors to form a tight focus in the crystal, with pump light injected through one or two dichroic mirrors. Some additional components such as mirrors and optical elements for wavelength tuning and/or ultrashort pulse generation are placed within the optical cavity. The laser crystal is usually quite small, typically with an optical path length of only a few millimeters [34].

Diode lasers are semiconductor laser devices based on laser diodes. Although the terms diode laser and laser diode are often used with the same meaning, it is appropriate to distinguish the terms: the diode laser is a laser device, which may sometimes consist only of a single laser diode [35]. A laser diode is a laser light emitting semiconductor device using the properties of a p-n junction [36]. Diode lasers may also contain additional items such as an external-optical resonator so that the device is an external-cavity diode laser or multiple laser diodes with some optics for beam combining.

3.2. GUNILLA

Ion Source

The ion source used at GUNILLA is a cesium sputter negative ion source of the model PS-120 from Peabody scientific [37] (see Fig. 3.2). It consists of a curved tantalum surface and a central aluminum rod which serves as an anode and cathode respectively [1]. Both surfaces are operated at a potential of 6 kV and the anode's surface rises its temperature to 1300 °C, while the cathode is at ambient temperature. The cesium reservoir container is heated up to 100 °C and provides the chamber with a hot vapour cesium cloud. The negative ions are accelerated towards the ionizer and extracted with a current of the order of μA to the magnet. Once they go through the mass selector magnet, the beam will be of the order of hundreds of pA to tens of nA.

Pulsing of the Ion Source

For the Au^- experiment there was a change on the ion source functioning. The pulsing mode of the ion source was introduced as a path towards the investigation of a cathode lifetime. A transistor switch was used, which is a fast high voltage switch from BEHLKE electronics (5 kV DC/30 A) [38]. This switch was integrated within the ion source and alters the sputtering voltage between -200 V and -3 kV. The time that the switch is on/off is determined by the repetion rate of the laser. Both, the transistor switch and the pulsed laser must be synchronised (see Fig. 3.3).

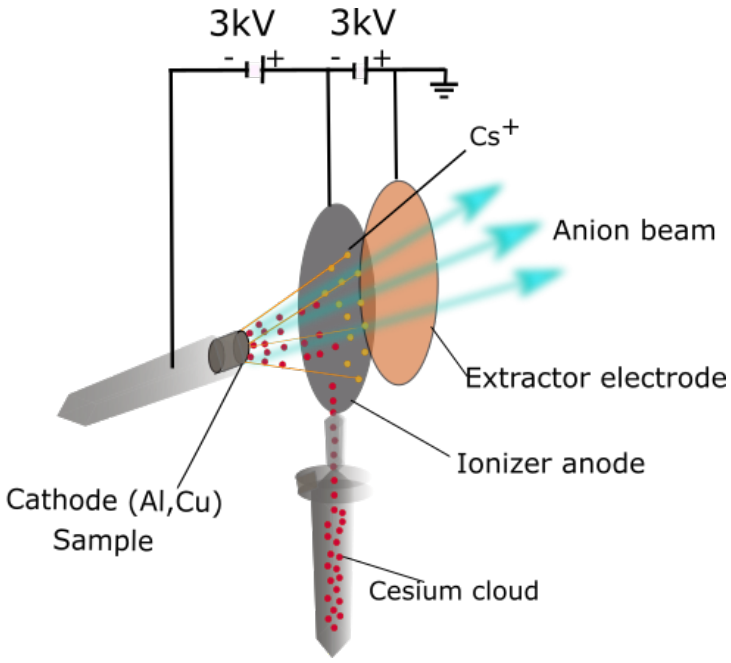

Figure 3.2: GUNILLA ion source. An Al or Cu base cathode is drilled with a sample powder. The Cs reservoir is heated up to 100°C. The Cs cloud evaporates and part of the Cs atoms get ionized on the ionizer surface, subsequently, they get accelerated towards the cathode surface by a potential difference of -3 kV, next, some Cs atoms form a condensate Cs layer. Atoms from the powder sample are sputtered after the Cs impact, where the Cs layer acts as electron donor for the sputtered atoms, which transform into negative ions. The negative ions are accelerated with 6 keV during extraction from the source.

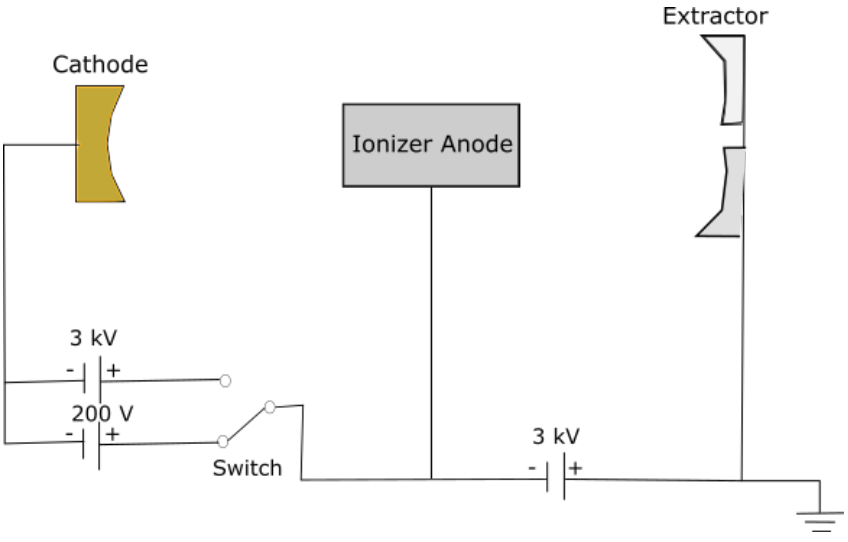

Figure 3.3: Scheme of the switch incorporated into the ion source.

GUNILLA Setup

The negative ions are created in the cesium sputter source that is connected to the selective magnet through the Einzel lens (see Fig. 3.4). It focus the beam towards the X lens which is used to focus the beam in the horizontal plane. At this stage of the path, a Faraday cup 1 (FC1) can be inserted into the beam. This is the first reference point. Once the beam goes through the magnet, it is possible to select the masses of interest for the photodetachment and after the magnet they drift towards the Y-lens, which focus the beam in the vertical direction [13]. Here, a second Faraday cup (FC2) can be inserted in order to monitor the mass selected current. Thereafter the ions pass a quadrupole triplet. This is a beam optic device used to focus the beam in x and y directions. Finally, the ion beam is deflected using quadrupole deflectors into the interaction region where it is overlapped with a laser beam. Both laser light and ion beam go through collimator 1 combined with collimator 2, which hence defines the interaction region. At this point, the Faraday cup 3 (FC3) is the reference point and finally the signal is detected by a Channeltron Electon Multiplier. A single turbo pump generates a source chamber vacuum of the order of 10^{-6} mbar, while the post magnet region runs in high 10^{-8} mbar, via another turbo pump [13].

The angle of intersection between the photons and the negative ion beam can be varied, where the most common angles are 90° (perpendicular), 0° (parallel) and 180° (antiparallel) [5]. In the experiments performed at GUNILLA, the 0° and 180° geometries were chosen because they result in a longer interaction path. For any of those methods, we must consider the time of flight, which is the time that the negative ions take to go from the negative ion source to the interaction region. This is calculated by $t_{TOF} = L/v$, where L is the distance of the path that the negative ions have to travel, and v is the velocity of the ions.

Channeltron Electron Multiplier (CEM)

To detect the electrons, protons and ions, an electron multiplier called channeltron detector is used (see Fig.3.5). In the front part of it, a low negative voltage is retained and at the back a high positive voltage is applied to accelerate the electrons through the channel until the end of the detector [9]. The input event reaches the front part of the detector creating secondary electrons which travel all along until the back of it creating more electrons. The unwanted signal is called noise and could be seen as dark counts or dark current. The first one, is caused by the collisions of negative ions with the residual gas, creating fast neutral atoms. The second one, is when the space among the electronic parts is too close, causing voltage arcing and crosstalk [9]. Images from the CEM could be appreciated in Fig. 3.5, 3.6 and 3.7.

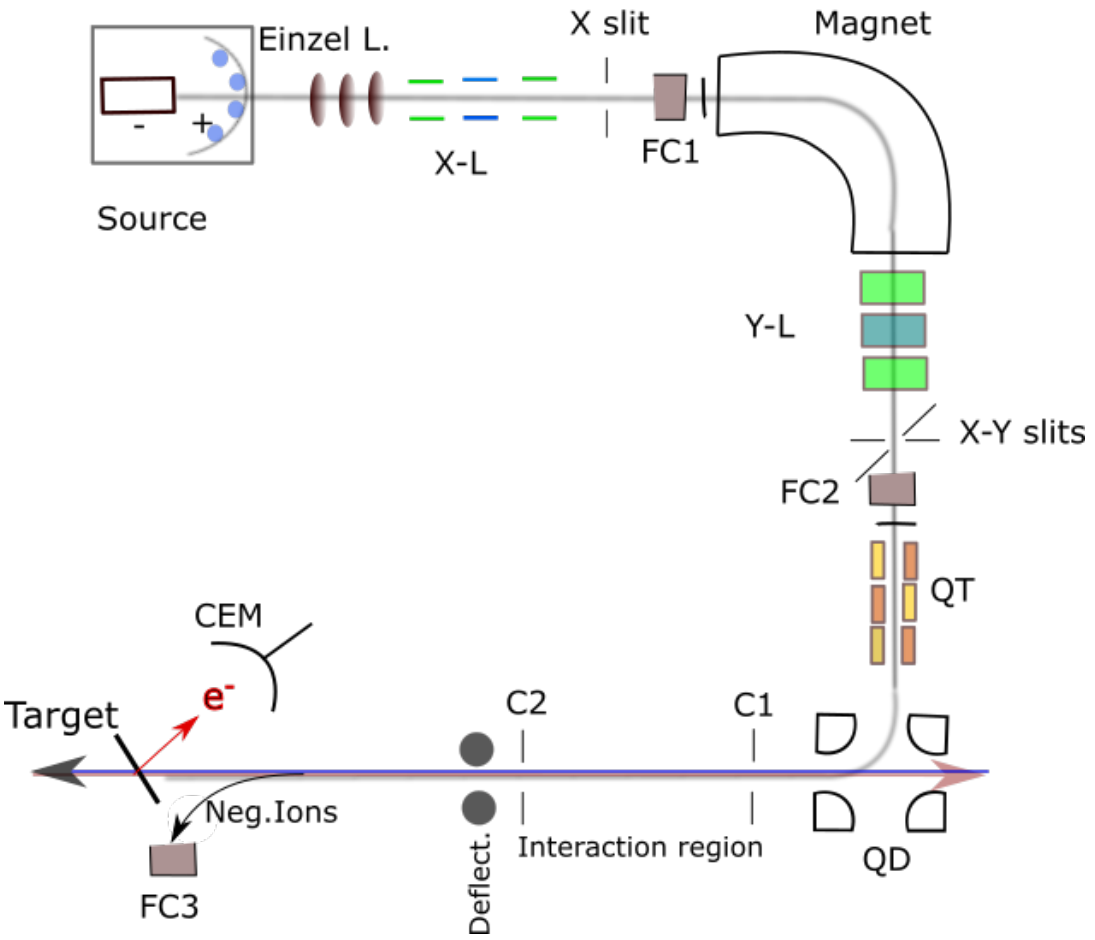

Figure 3.4: Gothenburg University Negative Ion Laser Laboratory (GUNILLA). Source, negative ion Middleton type source. Einzel lens (Einzel L.). X lens (X-L). X slit. Faraday cup 1 (FC1). Magnet. Y lens (Y-L). X and Y slits. Faraday cup 2 (FC2). Quadrupole triplet (QT). Quadrupole deflector (QD). Collimator 1 (C1). Collimator 2 (C2). Interaction region. Deflectors (Deflect.). Target. Faraday cup 3 (FC3). Channel Electron Multiplier (CEM). Electrons (e^-). The red and the blue arrows represent the laser beam sources going through and superimpose the ion beam in a parallel and antiparallel scheme. Color online.

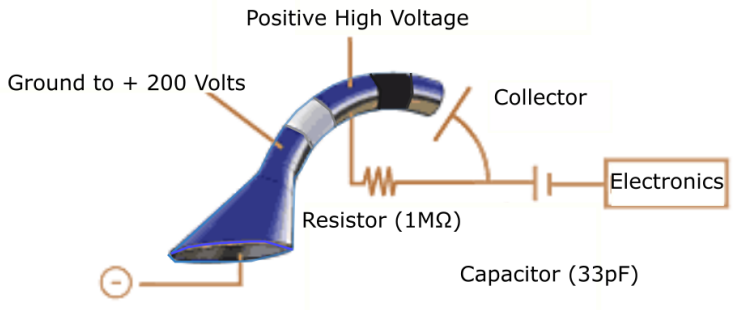

Figure 3.5: Channeltron Electron Multiplier configuration scheme used to detect electrons [9].

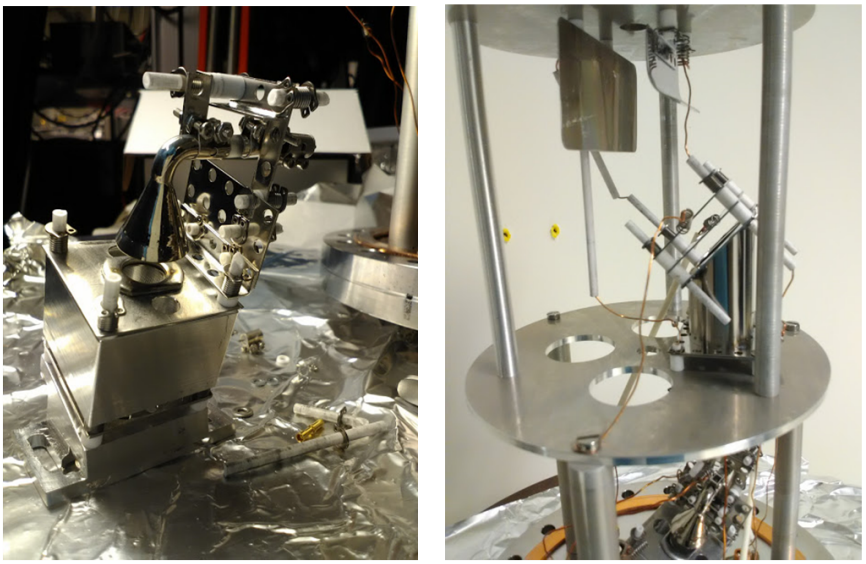

Figure 3.6: Left image: detector installation process. Right image: Faraday cup 3 (FC3).

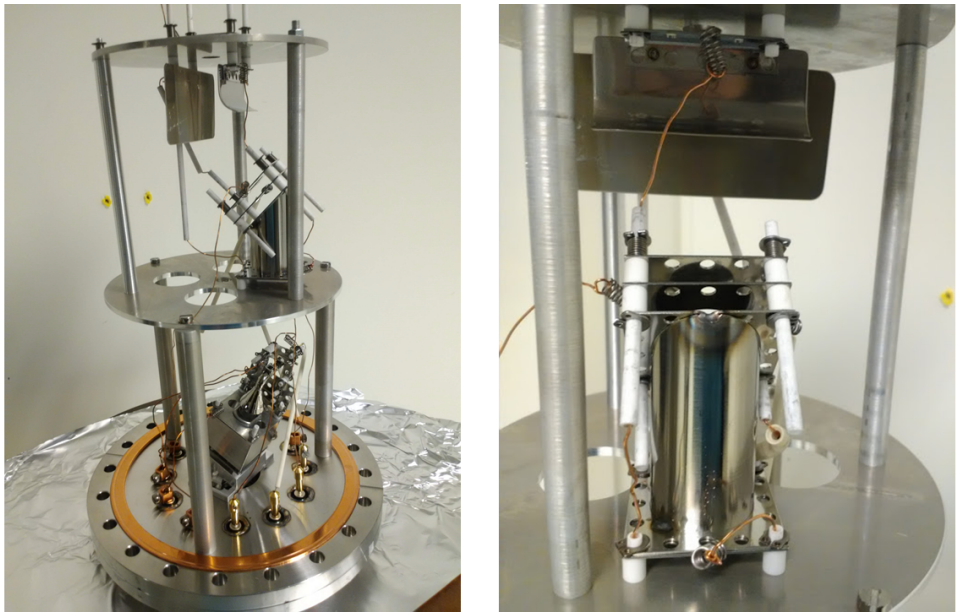

Figure 3.7: Left image: detector installed. Right image: Back perspective of the Faraday cup 3 (FC3).

Data Analysis at GUNILLA

Measurements at GUNILLA show neutral count rates normalized to count rates of the element under study on applied laser wavelengths. Normalized count rates were calculated using

$$Normalized\ Counts = \frac{Counts(A) - Counts(B)}{P \cdot C} \tag{3.6}$$

where *Counts(A)* and *Counts(B)* are registered counts in both windows accumulated, P is the mean recorded laser power, and C the mean ion current [21, 28].

For the data analysis of Au^- the set of data was given in energy in eV, the laser power in W, the ion current in nA, the total counts depend on the succesful number of events. Counts given as photodetachment are designed as Counts A and the ones given as background are known as counts B.

The fit function code in the appendix shows the error function for these measurements as

$$\begin{aligned} error\ CountsA &= \sqrt{CountsA}, \\ error\ CountsB &= \sqrt{CountsB}, \end{aligned} \tag{3.7}$$

where

$$\begin{aligned} error\ (Counts\,A - Counts\,B) &= \sqrt{[(error\ Counts\,A)^2 + (error\ Counts\,B)^2]}, \\ error\ (Counts\,A - Counts\,B) &= \sqrt{(\sqrt{Counts\,A})^2 + (\sqrt{Counts\,B})^2} \\ error\ (Counts\,A - Counts\,B) &= \sqrt{Counts\,A + Counts\,B} \end{aligned} \tag{3.8}$$

that are obtained under the assumption of a Gaussian probability distribution and then are normalized to laser power and ion current.

The fit function to Wigner's law is given by

$$Fit\ function = A + B(x - E_0) + |x - E_0|^{l+\frac{1}{2}}, \tag{3.9}$$

where l takes the values of l=*0* for an s-wave in case of arsenic and l=*1* for a p-wave in case of gold.

For the electron affinity, the *Fit function* was used and E_0 is the EA value. The fit function gives two values for E_0, one smaller than E_0 and one bigger: $E1_0$ and $E2_0$. Then,

a confidence interval CI is settled depending on the precision of the measurements, in this case, 0.67, and the two values of CI are subtracted from $E1_0$ and $E2_0$ respectively

$$|E1_0 - CI_1|,\ |E2_0 - CI_2|. \tag{3.10}$$

Subsequently, a maximum value is selected

$$max\left(|E1_0 - CI_1|,\ |E2_0 - CI_2|\right). \tag{3.11}$$

Finally, the maximum value is the EA error.

Lasers

At GUNILLA we used two OPO laser systems that are pumped with two Q-switched nanosecond Nd-YAG lasers.

The Laser Vision with OPO and OPA systems gives light in the range of 1350 nm and 5000 nm. It was used to study photodetachment of arsenic. The Spectra Physics MOPO system was used for the investigation of gold using a wavelength of 537.329 nm in the signal mode with 0.064 W-0.048 W of power. The system houses a master oscillator and a power oscillator (ergo, MOPO) and it uses a Type I beta barium borate (BBO) crystal as its nonlinear parametric gain medium [33]. This laser has an additional frequency doubling option (FDO) of the signal and idler modes, which make it possible to create light in the wavelength range from 220 nm to 1800 nm. Hence, the two systems combined cover the region of soft UV and MID IR [2].

3.3. NAPS

Ion Sources

NAPS setup consists of two ion sources, one that produces positive ions and the second one that produces negative ions.

The positive ion beams are produced by an Electron Cyclotron Resonance Source (ECR) using full permanent magnets of 2.45 GHz of frequency and 87.5 mT [39] for multiply charged ions, in which six magnets are ring-shaped to establish the axial confinement of the plasma electrons. This type of source was constructed in 2001 at the University of Bern and inherited from Giessen.

For the negative ion beam, a sputtering ion source was installed which is conformed by a cathode that is isolated from the source body. A cesium furnace is located right above the ionization chamber where a magnet provides a magnetic field. The ionization chamber contains two filaments. Finally, an independent limiting system allows precise control of the cesium flow and prevents the tube from cooling and becoming blocked when the source is stopped.

In the ion source, the cesium is heated between 95 °C and 105 °C in the oven and the resulting vapor enters the ionization chamber (see Fig. 3.8). This is brought to the same voltage as the anode, positive with respect to the cathode voltage. In this chamber where a magnetic field reigns, filaments create electrons. This magnetic field causes them to take a longer path which increases their probability of colliding with a cesium atom. Thus the number of ionized cesium atoms increases. The Cs^+ ions are then accelerated towards the target thanks to a potential difference between the anode and the cathode. By striking it, they will release a large number of negative ions which are extracted thanks to the potential difference. We thus create a beam of negative ions, whose energy depends on the potential of the cathode.

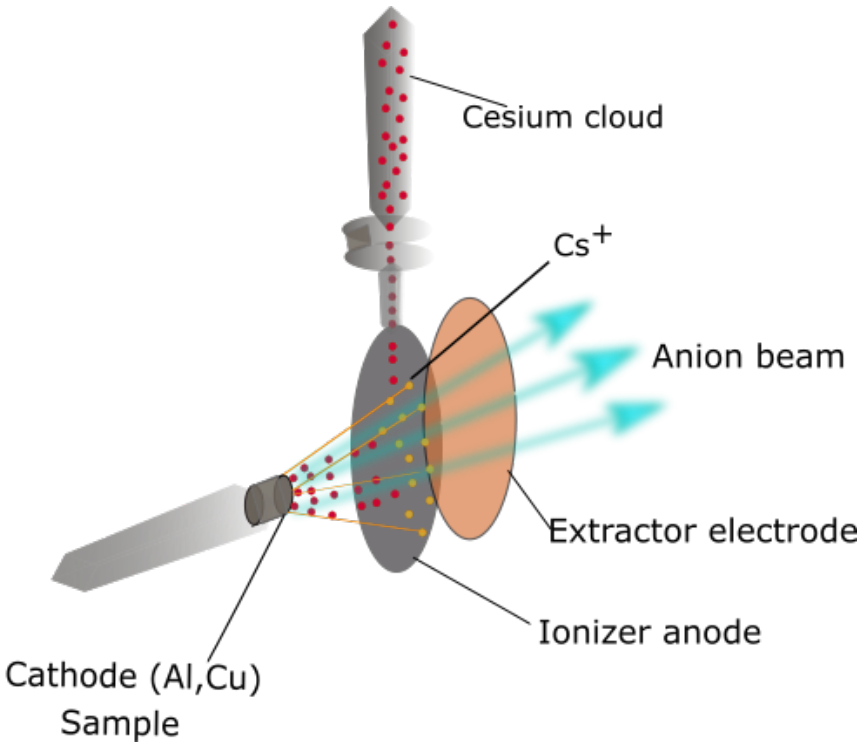

Figure 3.8: NAPS Negative Ion Source.

NAPS Setup

The first section includes two ion sources and optical elements which allow the beams to be routed to the interaction region. The detectors, labelled with an H are in the horizontal plane, while those labelled with V have an action in the vertical plane (Figure 3.9). The sources are each followed by an acceleration column with cylindrical symmetry comprising a double extraction electrode and a focusing lens. Then, in each of the channels, horizontal and vertical action deflectors ensure a first correction of the path of the beams.

In the negative beam side, the beam enters a large vacuum chamber. It is divided into two sections. The first element of the negative ion beam goes through a Wien filter which is a velocity selector. It consists of a perpendicular electric and magnetic fields which selects the charged particles based on their speed. Then follows a cylindrical deflector at 45° which gives the beam the right direction to cross the first diaphragm. After this, the beam passes through a horizontal detector HD1 and a vertical deflector VD1. In the positive beam side, a pair of horizontal and vertical deflectors makes it possible to align the beam to the magnet axis at 30°, which ensures the mass selection of the ions. Subsequently, after a vertical deflector correction, the beam passes through a spherical deflector at 45° and crosses a second diaphragm. Following this, it goes through a lens, a horizontal deflector HD2 and a vertical detector VD2. On each of the two channels, the detectors are followed by a rotating probe which can either intercept or allow the beam to pass depending on the position of its axis of rotation. This probe is followed by two diaphragms of 2 mm each, which will determine the final size of the beams. They precede two vertical detectors (VD1 and VD2) and two horizontal detectors (HD1 and HD2). The last two form, with another horizontal deflector (called mixer deflector), the beam tracking system. Finally, a small cubic aluminum cavity connects the deflectors to the collision region in which the two beams are brought together.

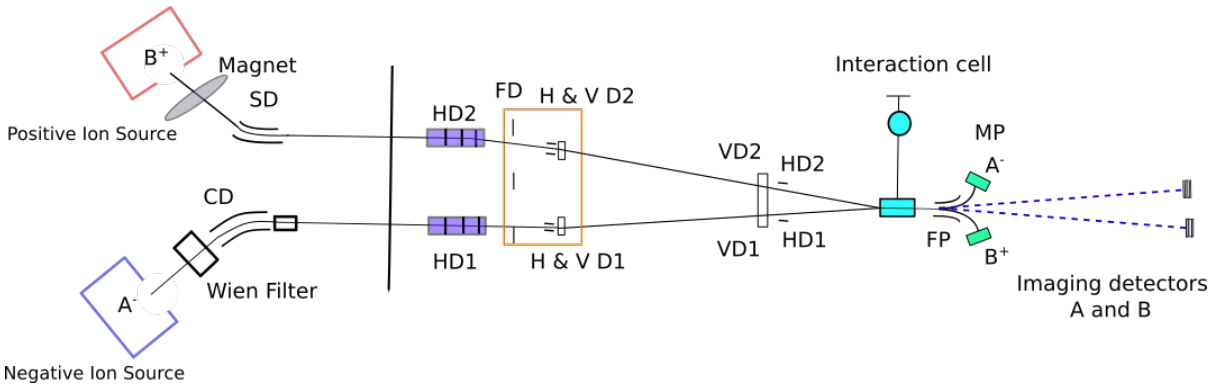

Figure 3.9: NAPS Scheme. Negative Ion source A^-, Positive Ion source B^+, Wien Filter, Cylindrical Deflector (CD), Spherical deflector (SF), Horizontal Deflectors (HD), Vertical Deflectors (VF), Fixed Diaphragms (FD), Interaction Region, Fixed Probes (FP), Mobile Probe (MP) and Imaging Detectors A^- and B^-.

Animated Crossed Beams Technique

The experiments performed at NAPS follow the Animated-Crossed-Beam technique (ACB) first proposed by Brouillard and Defrance [40], for electron-ion collisions and subsequently applied to one-photon light-matter interactions. The method was used to measure the absolute cross sections of Ag^- and Au^-. In the most of the experiments with crossed beams the absolute measurement of cross sections could suppose a certain profile for the beams. In laser beam experiments a Gaussian profile tends to be the assumption for a laser and a uniform profile in the case of the ion beam.

In ACB, instead of using two static beams, one of them moves across the other. The cross section dependency on both beams is erased when the signal is integrated over the beam displacement, leaving only integrated quantities to be measured. The mathematical development below has as reference the work of M. Génévriez and X. Urbain (2015) [41].

First, we start with the ionization probability

$$P(y,z) = 1 - exp\left[-\int \sigma\Phi(x,y,z)\frac{dx}{v}\right], \tag{3.12}$$

where v is the ions velocity, σ is the detachment cross section, and Φ is the photon flux in a determined (x,y,z) position.

Considering the linear nature of photodetachment, at low laser intensities the exponential of the above equation could be expanded in terms of power series. Then, taking into account only the first two terms, we have a linear relation between the detachment probability and cross section. The detector count rate N is the detachment probability, which is averaged over the ion beam section S and weighted by the detection efficiency η

$$N \simeq \sigma\,\eta \iint_S \frac{j(y,z)}{e}\left[\int \Phi(x,y,z)\frac{dx}{v}\right] dy\,dz, \tag{3.13}$$

where $j(y,z)$ is the current density at a (y,z) ion beam position and e is the elementary charge. The variable $N(Y)$ is measured as a function of the vertical displacement Y of the laser beam. Now, integrating over Y, we have

$$\int N(Y)\,dY \simeq \frac{\sigma}{e}\frac{\eta}{v}\iint_S j(y,z)dy\,dz \times \iint \Phi(x,y-Y,z)dx\,dY. \tag{3.14}$$

Here, Y is the vertical displacement of the laser, y is the vertical position of the ion

beam. As the photon flux Φ is the rate intensity of the laser to the photon energy $\hbar\omega$, the second integral is the laser power over $\hbar\omega$, which is independent of z. The integral of $j(y, z)$ is the ion current. Then the absolute cross section is given by

$$\sigma_{abs} \simeq \frac{ev}{\eta} \frac{\hbar\omega}{I_{ion} P_{laser}} \int dY N(Y), \tag{3.15}$$

where v is the speed of the ions, η is the detection efficiency, $\hbar\omega$ is the photon energy, and e is the elementary charge [15].

In the experiment the detachment rate is measured by a rotating glass plate at different angles. In addition, a razor blade is used to measure the vertical displacement dy, which corresponds to the increasing angle; the razor blade is placed after the rotating glass plate. By measuring the transmitting intensity as a function of the razor blade, one can obtain the vertical position of the center beam.

The Animated Crossed Beams setup is shown in Figure 3.10. Here we can see the perpendicular geometry between the negative ion beam and the laser light.

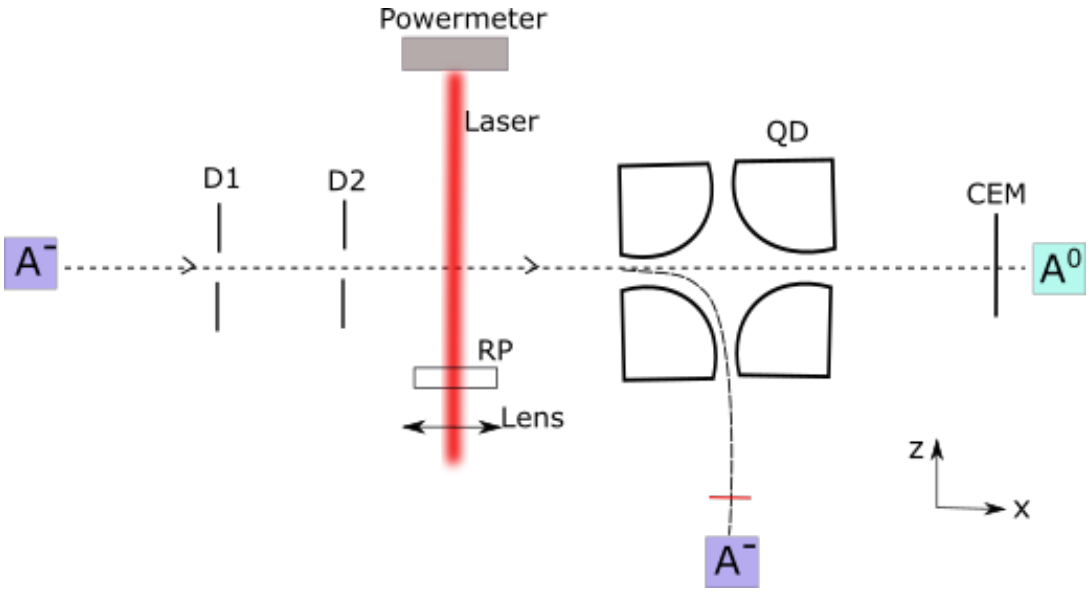

Figure 3.10: Animated Crossed Beams setup, Circular diaphragm (D1), Rectangular diaphragm (D2), Rotating glass plate (RP), Quadrupole deflector (QD), Channeltron Electron Multiplier (CEM).

Data Analysis at NAPS

Measurements at NAPS are based on the measurements of the static cross section, which computes the cross section for a static scan multiplicated by a form factor [42].

Then, the absolute cross section could be computed as

$$\sigma_{abs} = [C_{scale}]\ [form\ factor], \tag{3.16}$$

where the so called C_{scale} is

$$C_{scale} = [v_{ion}]\ [h\nu]\ \frac{1}{[N_{ion}][eff_{mcp}]}, \tag{3.17}$$

where the $v_{ion} \backsimeq 2{,}5\times10^{5}\frac{m}{s}$ is the ion velocity, $h\nu$ is the photon energy, $N_{ion} = 1\times10^{-12}\frac{1}{eV}$ and eff_{mcp} is the CEM efficiency is taken as 0.94 [43].

The *form factor* depends on various variables such as signal, the ion current, and the vertical displacement of the laser, these ones are manipulated through the trapezoidal rule

$$form\ factor = trapz\left(signal * \frac{1}{current\ * energy}, vert\right) \tag{3.18}$$

where the *trapz* function is an integral function for the trapezoidal method, *signal* is the number of counts when the laser is on, *current* is the correspondent ion current and *energy* is determined by the laser, *vert* is the vertical displacement which will be explain next.

The vertical displacement calculation depends on the angle respect to the ion beam, the wavelength, and the rotating glass plate (RP in Fig. 3.10). At this point, the vertical displacement is computed from the angular one. We have to take into consideration the position change of the laser beam when it is redirected towards the interaction region. Its position change as it came through optical mirrors and, subsequently its vertical displacement has to be calculated with the help of the angular displacement.

$$vert = [v_{ion}]\ [h\nu]\ \frac{d}{\sqrt{1-\left(\frac{sin\theta}{n_{refr}}\right)^2}} * sin\left(\theta - arcsin\left(\frac{sin\theta}{n_{refr}}\right)\right), \tag{3.19}$$

where d is a differential value of the vertical direction, y, θ is the angle between the ion beam and laser beam and n_{refr} is a function dependent on the rotating glass plate and the wavelength.

Finally, the error of σ_{abs} is given as

$$\delta\sigma_{abs} = \sqrt{\frac{C_{scale}^2}{n_{pulses}} \left(\frac{signal * \delta_{vert}^2}{(current * energy)^3} + \frac{K * \delta_{vert}^2}{(current * energy)^2} \right)}, \tag{3.20}$$

where K is an scalar used as an adjustment parameter for the variables before mentioned, n_{pulses} is the numbers of sweeps per measurement and $\delta vert$ is the error related to the vertical displacement of the laser, which depends on the angle between the ion and laser beams and the rotating glass plate.

Lasers

The lasers used at NAPS were a DPSS laser (Verdi-V10, Coherent) that provides light at a wavelength of 532 nm [44] and a diode laser (CNI, MDL-III-405) at 405 nm [45]. The first one is suited for Ti:Sapphire pumping. It has a single longitudinal mode ring cavity architecture enabling single frequency applications.

Channeltron Electron Multiplier

The Channeltron Electron Multiplier used at NAPS for one photondetachment is the model Sjuts KBL25RS with a typical ability to increase the signal at 2.3 kV applied voltage (see Fig. 3.11).

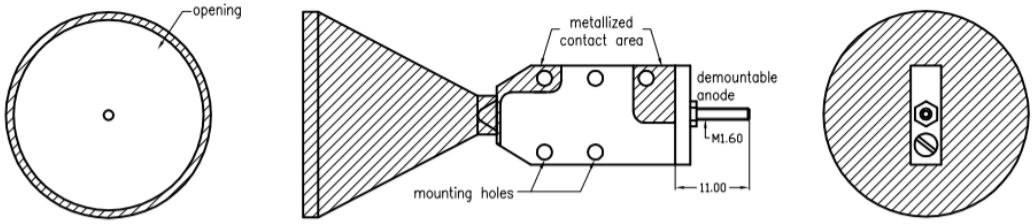

Figure 3.11: Channeltron Electron Multiplier (CEM), model Sjuts KBL25RS used at NAPS [43].

Chapter 4

Results

In this chapter the results obtained from the experiments performed at the Gothenburg University Negative Ion Laser LAboratory (GUNILLA) and at the Research du Cyclotron in the Nanoscopic Physics group (NAPS) of the Catholic University of Louvain La Neuve in Belgium are presented in two separate sections. All data analysis has been made in Python, EasyPlot and MATLAB.

4.1. GUNILLA

The experiments performed at GUNILLA were done with the purpose of measuring the electron affinities of arsenic and gold.

4.1.1. As^-

For the arsenic experiment, the measurements were done for one of the threshold $J = 2$ whose energy is 0.8048(2) eV with a wavelength of 1541 nm, showing a s-wave transition.

The laser that covers the range for this element was Laser Vision (OPO/OPA laser) and it was used to do antiparallel photodetachment from 1525 nm to 1555 nm with a 0.5 nm step size in the broad band mode.

The values for the EA of As in Tab. 4.1, show firstly, the value without Doppler Shift,

Electron Affinity	
$EA_{Arsenic} = 0.8048(4)$ eV	Without Doppler Shift
$EA_{Arsenic} = 0.8045262(2)$ eV	Corrected for Doppler Shift
$EA_{As_{Ref}} = 0.8048(2)$ eV	Measured by Walter *et al.* [22]

Table 4.1: The measured $EA_{Arsenic}$ is shown in this table. First, we provide the $EA_{Arsenic}$ obtained at GUNILLA without correction for Doppler Shift, in addition we have the value corrected for Doppler Shift. These values are compared to the experimental data obtained by Walter *et al.* [22].

then this one was corrected and finally both of them are compared to the experimental data obtained by Walter *et al.* [22].

In Fig. 4.1, we show the final experimental data of the analysis, where the continuous line is the analytical fit curve to Wigner's law, where for an s-wave transition $l = 0$ and thus we have: $\sigma(E) \approx C(E - EA)^{\frac{1}{2}}$, where E is the photon energy of the laser and EA is the electron affinity and C is the amplitude of the function. The vertical dashed line shows the EA with the Doppler Shifted value obtained at GUNILLA, while in the s-wave threshold fit curve we can see the value for the experimental data obtained by Walter *et al.* [22].

For further analysis, the data was normalized to laser power and ion current as seen in Eq. (3.7), and the error propagation is given by Eq. (3.9), the data was consequently fitted to a single Wigner's law fit in order to determine the Doppler shifted EA. The resulting fit is presented in Fig. 4.1.

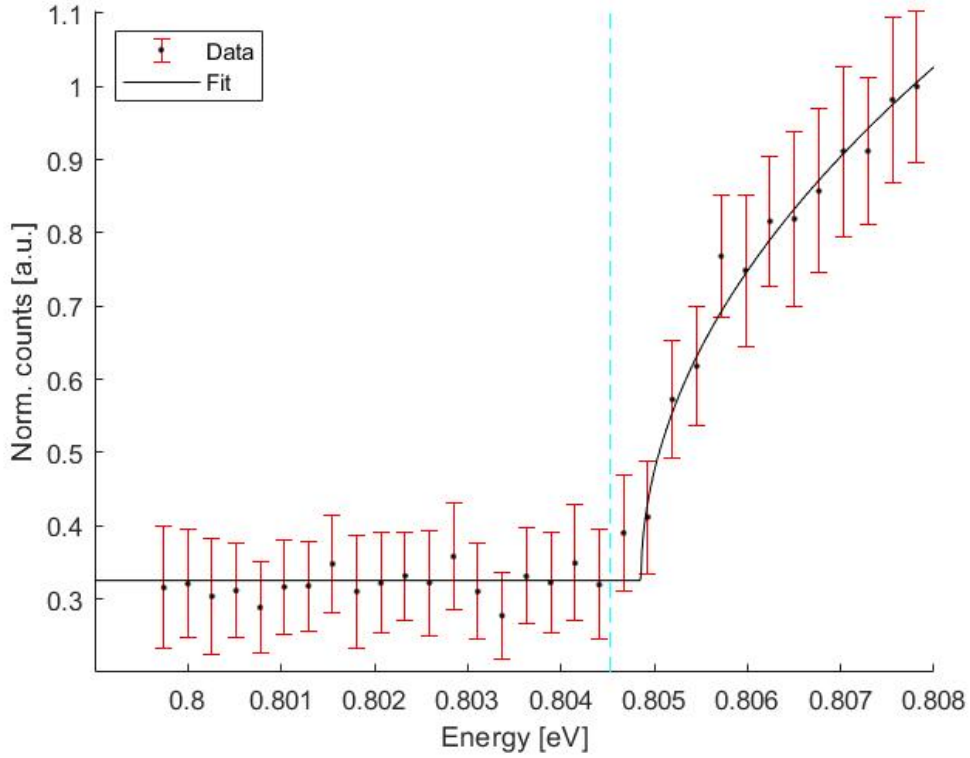

Figure 4.1: As^- photodetachment data taken in antiparallel geometry at GUNILLA. The figure shows an *s*-wave transition with the EA value at 0.8045262(2) eV corrected for Doppler Shift (vertical dashed line), while the literature shows the threshold at 0.8048(2) eV based on the work of Walter *et al.* [22].

4.1.2. Au^-

For the gold experiment the MOPO laser was used in the range between 530 nm and 544 nm. In this experiment, the pulsing mode of the ion source was introduced to extend the cathode's lifetime.

The ion source is pulsed at 10 Hz, making each cycle 0.1 s = 100 ms long. The "duty cycle" is the fraction of time the switch is on. For the gold experiment a 10 % duty cycle was used. This means that throughout 100 ms, the switch is on for 10 ms and off for 90 ms.

The switch is operated at two different voltages: -3 kV and -200 eV. The last one is the difference between the ionizer anode and the extractor electrode making the process of extraction different to the normal one. When the laser is on, the lamp takes 174.1 μs to send the laser pulse, while triggering the source takes 80 μs to have the peak of the ion beam (see Fig. 4.2). Both pulse and ion peak have to arrive at the same time to have

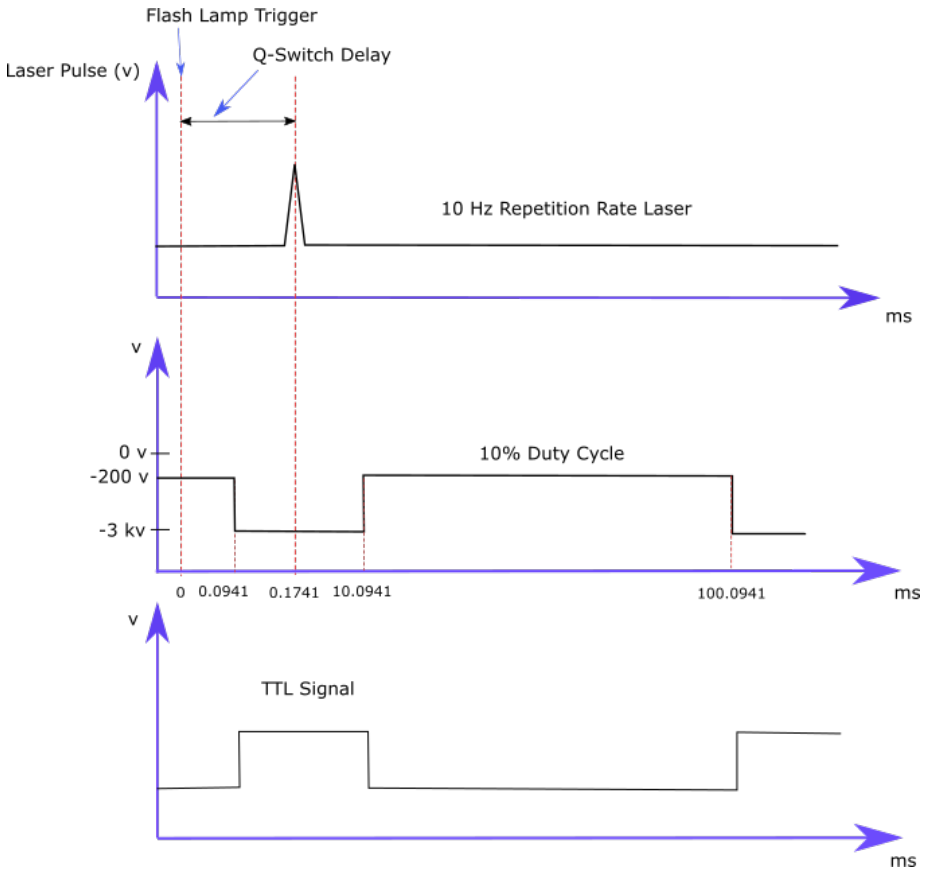

Figure 4.2: 10 % duty cycle. The ion source is pulsed at 10 Hz. Each cycle is 0.1 s = 100 ms. For the gold experiment, the switch is on for 10 ms.

photodetachment. This means, we have to set a delay in the source. Once the laser is on and when there is 80 μs left, the source is triggered by the laser via the laser lamp. Subsequently, the source is activated and it is on for 10 ms.

The signal is received in the oscilloscope as we can see in Fig. 4.5, where the light blue line represents the established gate to acquire the photodetachment signal. The yellow line represents the signal from the CEM, better known as counts. The pink line corresponds to the trigger pump signal from the laser and the dark blue line corresponds to the pulse generator, thus it represents the pulses.

A comparison of different events in the signal detection is shown in the following figures. In Fig. 4.3 is shown the oscilloscope before the detection of the photodetachment signal. Here the ion beam and laser beam are blocked, i.e, none of them goes in the interaction region. Fig. 4.4 shows collisional detachment when the ion beam reaches the detector while there is no laser beam. Fig. 4.5 shows photodetachment signal when both, ion beam and laser beam are unblocked. Here the photodetachment signal is detected inside the gate.

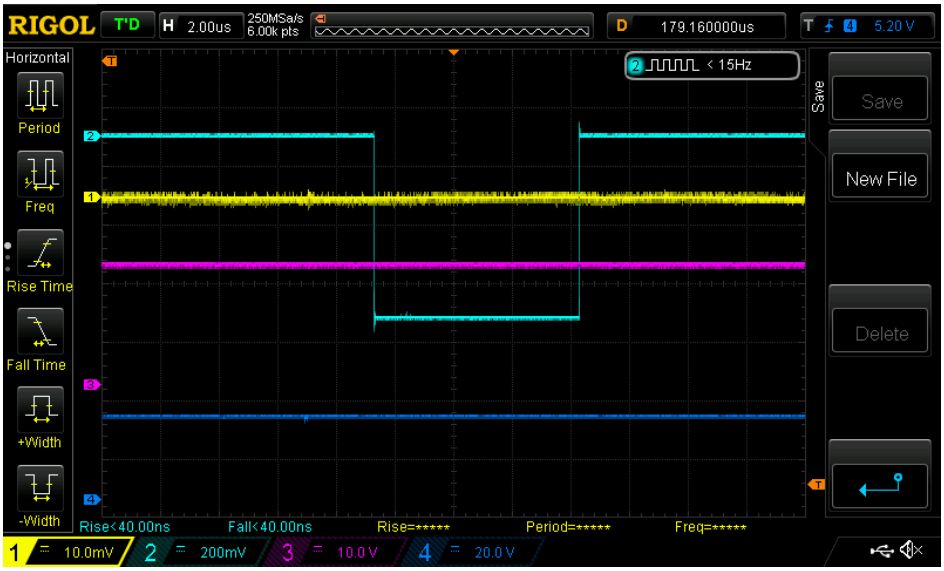

Figure 4.3: (Color on-line). Au^- experiment. Light blue line: gate that detects the photodetachment signal. Yellow line: collisional detachment signal (out of the gate) and photodetachment signal (inside the gate). Pink line: laser pump connection. Dark blue line: pulse generator connection. Here both the ion beam and laser beam are blocked.

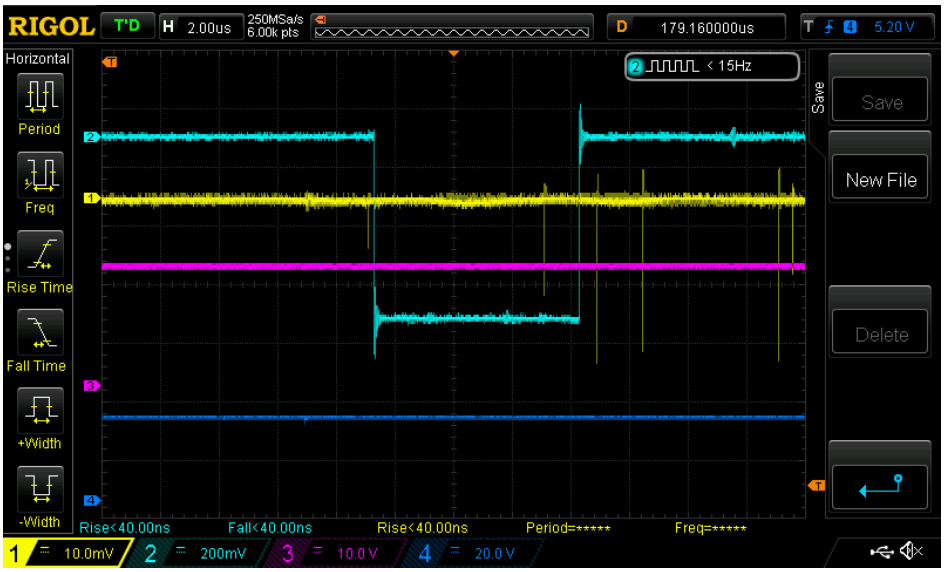

Figure 4.4: (Color on-line). Au^- experiment. Oscilloscope signal while there is ion beam and the laser is blocked. We see no collisional detachment or photodetachment signal in the yellow line.

The data for the gold experiment at GUNILLA was taken at 1 nm step size from 530 nm to 544 nm, where the ion source was pulsed between -200 eV and -3 kV. The data was normalized to laser power and ion current as seen in Eq. (3.7), and the error propagation is given by Eq. (3.9), the data was consequently fitted to a single Wigner's law fit, where

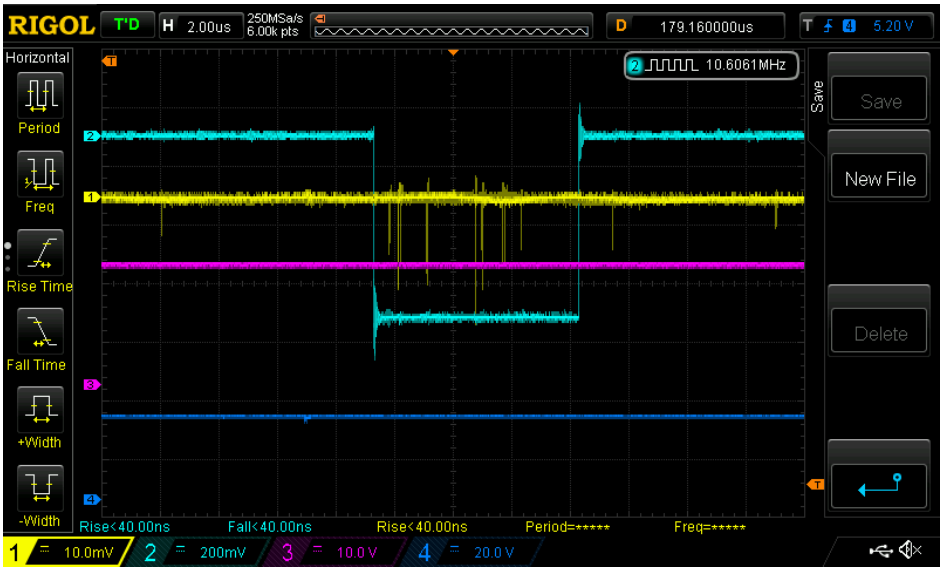

Figure 4.5: (Color on-line). Au^- experiment. Oscilloscope signal when there is ion beam and the laser are unblocked, here the photodetachment signal is visible on the screen (inside the light blue gate) and collisional detachment is outside the gate.

the data fitted to a p-wave transition $l = 1$ and thus we have: $\sigma(E) \approx C(E-EA)^{\frac{3}{2}}$, where E is the photon energy of the laser and EA is the electron affinity and C is the amplitude of the function. The resulting fit is presented in Fig. 4.6. The different values for the EA are shown in Tab. 4.2 where the error propagation for the Doppler Shifted value come from Eq. (3.4). The vertical dashed line in Fig. 4.6 shows the Doppler Shifted value for the EA obtained at GUNILLA, while the EA value from Andersen *et al.* presented a threshold before this line, mofe specifically at 2.30861(3) eV. The difference between the reference and the experimental value obtained at GUNILLA suggest the necessity of taking more measurements to improve the final experimental result.

Electron Affinity	
$EA_{Gold} = 2.316(1)$ eV	Without Doppler Shift
$EA_{Gold} = 2.316592(4)$ eV	Corrected for Doppler Shift
$EA_{Au_{Ref}} = 2.30861(3)$ eV	Measured by Andersen *et al.* [12]

Table 4.2: The measured EA_{Gold} is shown in this table. First, we have the EA_{Gold} without correction for Doppler Shift, then we have the value corrected for Doppler Shift and finally we have the value from literature measured by Andersen *et al.* [12]

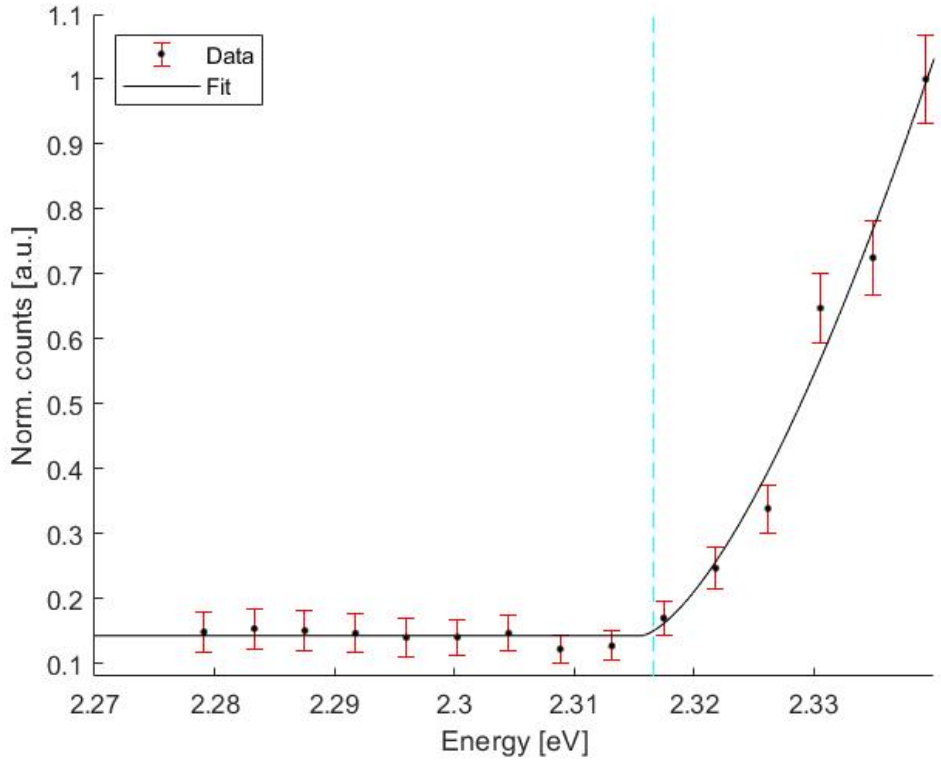

Figure 4.6: Au^- photodetachment data taken in a parallel geometry with the pulsing mode of the ion source.The figure shows a p-wave transition with the EA value at 2.316592(4) eV corrected for Doppler Shift (vertical dashed line), while the literature shows the threshold at 2.30861(3) eV based on the work of Andersen *et al.* [12].

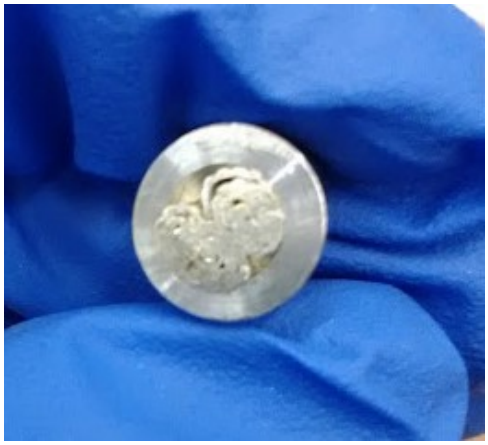

Figure 4.7: Al base cathode with a rolled sample of silver plate.

4.2. NAPS

The experiments at NAPS required a temperature between 95 °C and 105 °C in the cesium reservoir of the negative ion source, and a vacuum of 1-2×10^{-6} mbar. Before doing the experiment the mass separator was calibrated using O_2.

4.2.1. Ag^-

For the silver experiment an aluminium base cathode was used. The silver sample could be in powder or in a solid form. In our case, both states were tested, finding that the solid sample (without baking it) gave the best signal.

The first try for the cathode's test was to prepare a tantalum surface by drilling a hole in the center, and attach it to the aluminium cathode containing the powder. The purpose of this technique was to get rid of the aluminum peaks in the mass spectrum, and obtain a beam containing only tantalum and silver. The second try was to use a cathode with a wider hole, so that the area of interaction was greater, facilitating the alignment of the optics. The third try was to fill a cathode with silver and bake it in order to have a cleaner and bigger peak of silver, this eliminates the oxygen remnants, but this was not successful. Finally, the cathode used was an aluminium base with a rolled silver plate in the center as shown in Fig. 4.7.

In order to stabilize the ion beam, a current of 0.18 mA in the cathode was needed. Once we had a stable ion beam, it was possible to observe laser induced neutral Ag impacts on one of the position sensitive detectors, which are normally out of axis.

The following figures 4.8 and 4.9 show the relation among mass spectrum, the time of flight of the elements under study, and the ion yields for every negative ion beam. No error propagation has been calculated for these graphs given that this is a visual representation of the comparison of the elements.

By performing the experiment with and without the Wien filter, we allow the detection of all the masses in order to have a spectrum and a reference of all the elements in the sample. This can be seen in figures 4.8 and 4.9 for the silver and gold samples.

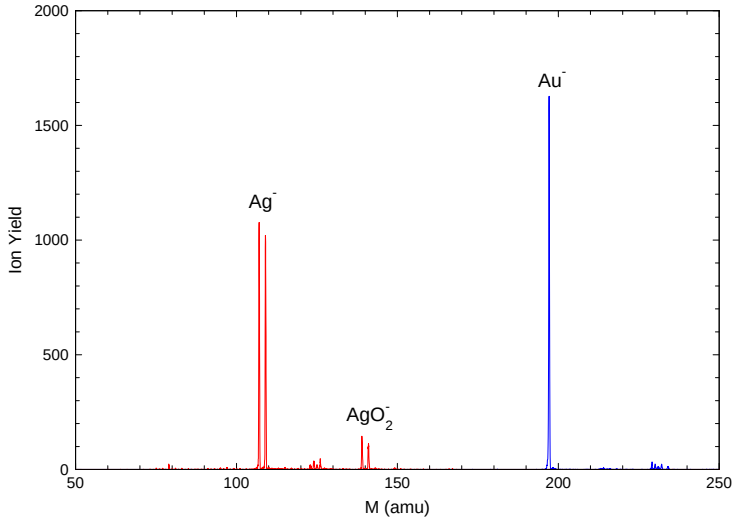

Figure 4.8: Mass spectrum. Ion yields for Ag^-, AgO_2^- and Au^-. Ag^-(107.868 amu), AgO_2^- (143.868 amu) and Au^- (196.9665 amu). Developed by NAPS, UCL 2020.

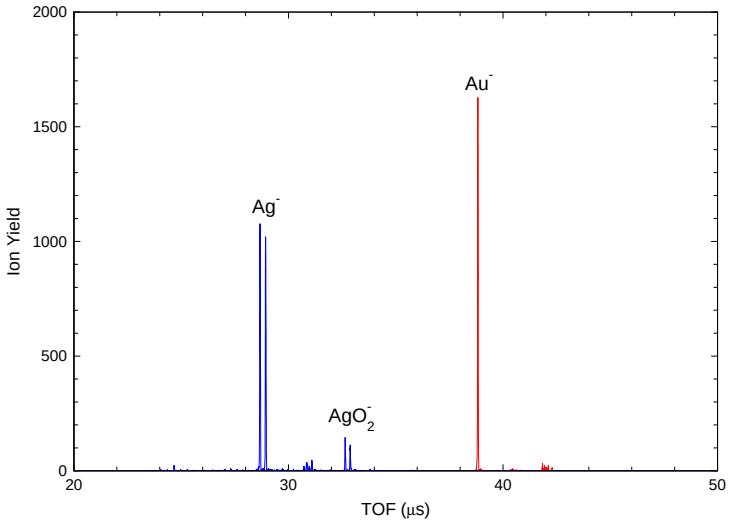

Figure 4.9: Time of flight spectrum of the negative ion beams and their respective ion yields. Ag^- (28.3, 28.5 μs), AgO_2^- (32.8, 32.9 μs) and Au^-(38.8 μs). Developed by NAPS, UCL 2020.

The photodetachment experiment was conducted using a DPSS green laser (Verdi-V10, Coherent) at a wavelength of 532 nm and a blue diode laser (CNI, MDL-III-405) at 405 nm. In order to lower the collision background and to limit detector aging, the anion beam is pulsed by switching on and off the deflector (D1) using a fast high voltage switch of 1 s (see Fig. 3.9). The ions pass to a Faraday cup when the deflector is off allowing the ion current to be detected. When the detector is on, ions pass through D1 and D2 and are collimated by two diaphragms housed in a rereferencing tube.

In Tab. 4.3 the absolute cross section values for Ag^- at 90 % confidence level are presented, here the measurements were performed by the ACB. Having a close look to Fig. 4.10, the reference data point obtained by Hotop *et al.* [27] was taken as our main reference and we can see that this point is on the calculation line presented by Amusia *et al.* [46]; on the other hand, σ_1 was obtained with a green laser of 2.33 eV, where the error line is on the solid line, σ_2 was obtained with a blue laser of 3.06 eV, nevertheless, the error bar of the latter is above the line, suggesting the measurements have to be improved.

Absolute Cross Section	Energy	Wavelength	Photon Energy
$\sigma_1 = (7.4\pm0.3)\times10^{-21}$ m^2	2.33 eV	532 nm	18796.99 cm^{-1}
$\sigma_2 = (5.4\pm0.2)\times10^{-21}$ m^2	3.06 eV	405 nm	24691.35 cm^{-1}
$\sigma_{ref} = (6.5\pm1)\times10^{-21}$ m^2 [27]	2.1 eV	590.4 nm	16900 cm^{-1}

Table 4.3: Absolute cross section for Ag^- with a green and blue laser, 532 nm and 405 nm respectively, compared to the value measured by Hotop *et al.* [27].

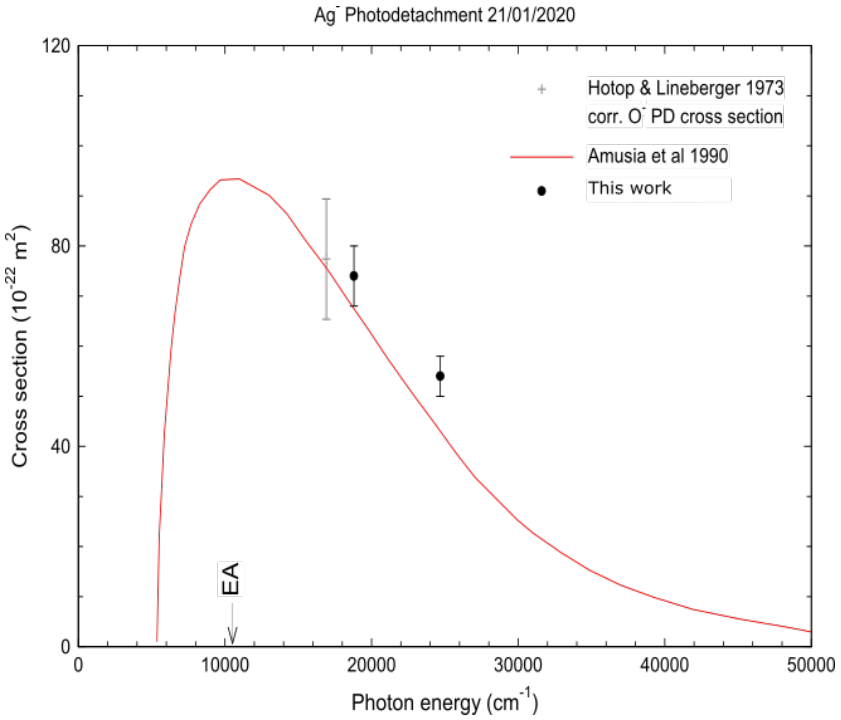

Figure 4.10: Ag^- Photodetachment. The measurent at 18796.99 cm^{-1} was recorded using the green laser, yielding a cross section of $\sigma_1 = (7.4\pm0.3)\times10^{-21}$ m^2. The measurent at 24691.35 cm^{-1} was recorded using the blue laser, yielding a cross section of $\sigma_2 = (5.4\pm0.2)\times10^{-21}$ m^2. The solid line is the calculation for absolute cross section for Ag^- made by Amusia *et al.* [46]. Developed by NAPS, UCL 2020.

In the following Fig. 4.11, the upper section corresponds to the additional neutrals that come from photodetachment, with the green laser. While, in the lower section corresponds to laser off for all neutrals. We see that they arise from collisions of $A^- + X \longrightarrow A + e + X$, where X is a molecule of the residual gas, most likely H_2. In the case of Ag^- (greatest peak in Fig. 4.11) we see very little neutrals produced by background collisions.

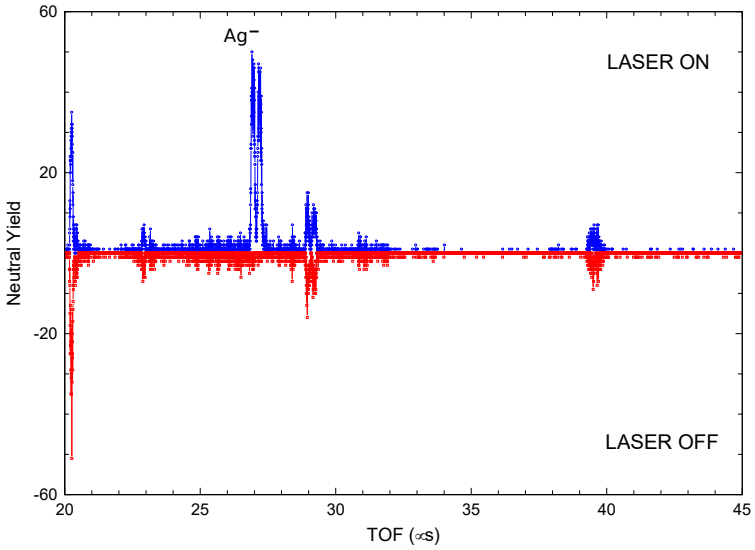

Figure 4.11: A comparison between laser on and off in the Ag^- experiment. The positive neutral yield (upper section) shows the additional neutrals from photodetachment. The negative neutral yield (lower section) shows the collisional detachment. Developed by NAPS, UCL 2020.

4.2.2. Au^-

For the gold experiment an aluminium base cathode was used. The gold sample was a solid and rectangular one as shown in Fig. 4.12.

Figure 4.12: Aluminium base cathode with a solid and rectangular gold sample.

Gold is very prolific in producing negative ions. Further, since it has only one isotope, there is no trouble in identifying the peak. The current rises rapidly (in minutes) and once it stabilizes, it is simple to align the optics to get the maximum output.

The photodetachment of Au^- was done is the same way as with silver, with both lasers, green and blue and with the same switching window for the deflector. The measured cross sections for Au^- are:

Absolute Cross Section	Energy	Wavelength	Photon Energy
$\sigma_1 = (0.62 \pm 0.04) \times 10^{-22}$ m^2	2.33 eV	532 nm	18796.99 cm^{-1}
$\sigma_2 = (44 \pm 0.95) \times 10^{-22}$ m^2	3.06 eV	405 nm	24691.35 cm^{-1}
$\sigma_{ref} = (2.6 \pm 30\,\%) \times 10^{-22}$ m^2 [27]	2.4 eV	523 nm	19120 cm^{-1}

Table 4.4: Absolute cross section for Au^- with a green and blue laser, 532 nm and 405 nm respectively, compared to the value measured by Hotop *et al.* [27].

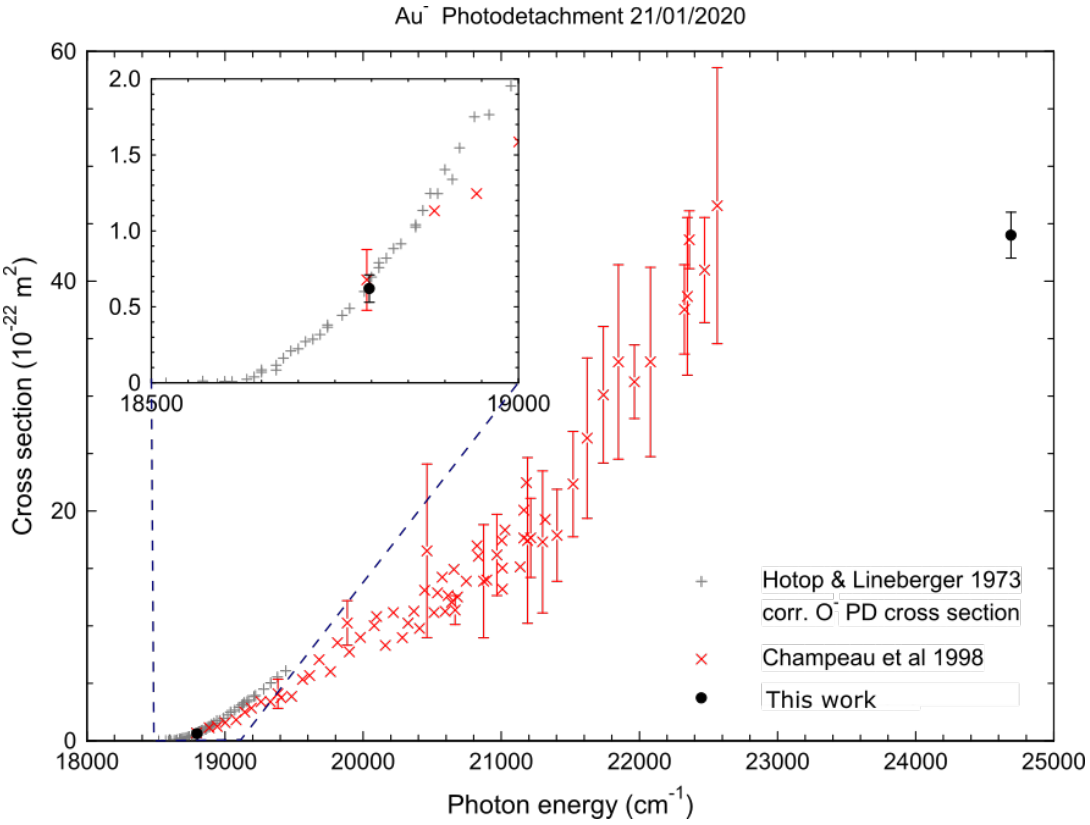

Figure 4.13: Au^- photodetachment cross section. The first point (inset) corresponds to the measurements done with the green laser and $\sigma_1 = (0.62 \pm 0.04) \times 10^{-22}$ m^2 and the second point corresponds to the ones done with the blue laser and $\sigma_2 = (44 \pm 0.95) \times 10^{-22}$ m^2. Developed by NAPS, UCL 2020.

Chapter 5

Technical discussion and conclusions

The results presented in this thesis are intended to help to answer the questions presented in the introduction and accentuate the importance of this research.

For the experiments performed at GUNILLA, the data was normalized to current and laser power. In the case of background signal, it could not be acquired and it was zero for the entire experiment. Unfortunately, the sample of arsenic in the cathode ran out after several days of measurements, not allowing for the improvement of the results. Despite of this, the acquired EA agrees with the experiments carried out by Walter *et al.* [22]. The future of the arsenic experiments is to perform parallel and antiparallel photodetachment scans measuring the thresholds for the excited states in As^- at 1831 nm and 1935 nm. Another improvement would be the measurements of the fine structure splitting of As^-, which require longer wavelengths. Furthermore, a modification in the cathode could be made by adding silver to the mixture. This frequently makes them run more steadily and causes the negative ion current to rise more quickly. Finally, the pulsing mode of the ion source could be added to extend the cathode lifetime and to maybe improve the amount of current produced in the process.

For the gold experiment, since it is a very prolific negative ion and since elemental cathodes performed so well, the obtaining of collisional detachment signal was very easy. Even though the current rises spectacularly within minutes, the acquisition of the photodetachment data was problematic due to the unstable behaviour of the MOPO laser. The EA results for gold show a p-wave detachment. However, an improvement in the value of the EA was not possible. The normalization for the data set was done for ion

beam current and laser power as done before with the arsenic results. Improvements for this experiment could be the parallel and antiparallel photodetachment with an upgraded MOPO laser and the high accuracy wavelength meter. Additionally, since the laser has a grating issue with small nanometer step size, it is recommendable to run the measurements with 1 nm stepsize from different starting points, normalize the data and to combine the data sets into one plot for measurements done in the same session.

For the experiments at NAPS it was possible to measure cross sections for Au^- and Ag^-, with the Au^- results we have the opportunity to compare it and the experimental technique with the ones obtained at GUNILLA. In both experiments it was easier to perform them with Au^- given the rapid rise of gold current and oxygen was used as a reference for its well known absolute cross section.

Finally, for the purposes in this thesis, the system at NAPS allows us to perform photodetachment experiments for absolute cross sections (in a 90° approach) and electron affinities. The ion source presents complications since the companies that used to export the spare parts do not produce them anymore, making the upgrading and maintenance of the source limited, since NAPS users are the ones who do it. The absence of a magnet at NAPS makes the selection of masses more difficult as the Wien filter does this part of the process. On the other hand, the system has a positive ion source that allows to make research in that field.

The system at GUNILLA allows to perform photodetachment experiments for relative cross sections in a parallel (at 0°) and antiparallel (at 180°) approach. It has a commercial negative ion source and a magnet that make it easier with the selection of the masses of interest. The resolution of troubles at GUNILLA is complicated given the complexity of disassembling the system. In the laser part, the laser assembly at GUNILLA has more options in which lasers can be used, while at NAPS, they have a simpler way of performing these measurements with Nd-YAG and Ti:Sa portable lasers.

The pulsing mode of the source made it possible to extend the gold cathode lifetime. While at NAPS, the cathode's lifetime was in average two days. The pulsing mode of the source in GUNILLA made the lifetime to extend to several weeks, allowing to find the most effective duty cycle and to perform LPT spectroscopy.

In the course of this thesis both systems were used for different outcomes. They have pros and cons making the way of performing the experiments in a very specific way in which they complement each other. In conclusion, the measurement of the electron affinities of As^- and Au^- and the photodetachment cross section of Au^-, and Ag^- were achieved at GUNILLA and NAPS under different experimental conditions. Our results compare well with the experimental and theoretical data available in the literature. For an undergraduate student, this has been an exceptional experience and has thought me how to carry out experimental work at high level experimental facilities.

Acknowledgments

There are many people who helped me during the development of this thesis and without them, it could not have been possible.

First of all, I want to thank Dag Hanstorp for being the most patient professor I have met in all my entire academic experience, for giving me the opportunity to do the experiments at GUNILLA and for facilitating the connections that allowed me to perform experiments at NAPS. I want to thank Remigio Cabrera Trujillo for choosing me to be part of the Linnaeus Palme program and for guiding me during the work of this thesis.

To Di Lu, who taught me the experimental methods at GUNILLA and the ones related with the lasers and for always helped me to solve many issues at the laboratory. To David Pegg, who spent a lot of his precious time explaining me the theory behind negative ions, for being a mentor, and a friend to me. To Brian Senabulya who helped me with some of the experiments presented in this thesis, but specially for being my friend and support when we experienced many difficulties. I won't forget the uncountable good moments we spent in the laboratory. To Jakob Welander who helped us solving the many issues we had at GUNILLA and with the detector.To Ademir who taught me about lasers. To Annie Ringwall-Moberg for her kindness and support and for helping me with the data analysis. To Jessica Warbinek for helping me with the pulsing mode of the source, for solving the most of my doubts and for helping me with the data analysis. To Mats for helping the negative ion team with his knowledge in technical and electronic matters. To Jan-Åke for manufacturing key configurations arrays at GUNILLA. From the Université Catholique de Louvain, I want to thank Xavier Urbain for being clear in his explanations about the experiment, for his patience and motivation for the atomic physics. To Arnaud Dochain who was the first one who made me understand the photodetachment process with his great ability to teach. Special thanks to Raphaël Marion who helped to analyse the data obtained at NAPS.

To the University of Gothenburg and UNAM for making possible this experience to learn and create scientific knowledge to students like me who otherwise would not have acquired in any other place.

To the Freden family: Guadalupe, Per, Victoria and Mikael, and to the Salgado Barrera family: Andrea, Pablo, Catalina and little Pablo for making me feel at home

when I was in Sweden and who helped me whenever I needed.

To all my friends, Eva Zeferino, Jennifer Meneses, Laura Spissinger, Carlos Leija, Lucero Morelos, Anel Ortiz, Sonia Korina, Brittany Cruz and Samara Vega, thank you for your friendship since immemorial times.

Special thanks to my friend and teacher Vladimir Lemus, for being of great help during the writing of this thesis and to my uncle Alberto Quintana, for listening and trusting me.

To my mom Martha Pérez Valadez, my dad Miguel A. Cruz López, my brothers Arturo Cruz Pérez and Miguel A. Cruz Pérez and to my aunt Lucila Pérez Valadez who have always believed in me and have gave me love and light to persist in the most difficult moments. Thank you for helping me to become the person I am today, for teaching me the real value of life, for making me love education and science. This thesis is for you, all my achievements are yours.

To my little nephew Santiago Émile, who makes me incredible happy every time I see him and who has always inspired me to become the best person I can be.

To my partner Ricardo Sánchez González, thank you for all your love, support and kindness. You have made me happier than ever. I am the best version of myself thanks to you.

Finally, I acknowledge the support from DGAPA-PAPIIT IN-111-820 project during the completion of this thesis.

Appendix

An extract of the data obtained at GUNILLA is shown in this section.

2020-03-27_As_1535_nm_noseeding_broadband
27/03/2020 13:35:25

Counts A	Counts B	Wavelength[nm]	Current[nA]	Power[W]
112.000000	0.000000	500.000000	0.026024	0.013840
126.000000	0.000000	500.000000	0.025977	0.013773
113.000000	0.000000	500.000000	0.025736	0.014148
110.000000	0.000000	500.000000	0.025671	0.013867
113.000000	0.000000	500.000000	0.025656	0.013985
123.000000	0.000000	500.000000	0.025396	0.013972
107.000000	0.000000	500.000000	0.025378	0.013947
92.000000	0.000000	500.000000	0.025337	0.013790
99.000000	0.000000	500.000000	0.025258	0.014118
98.000000	0.000000	500.000000	0.025024	0.014067
108.000000	0.000000	500.000000	0.024979	0.014086
100.000000	0.000000	500.000000	0.024854	0.013756
116.000000	0.000000	500.000000	0.024748	0.014218
94.000000	0.000000	500.000000	0.024763	0.013970

Figure A1: Fine scan on the As target, no seeding broadband 1 nm step size.

2020-03-30_As_1535.5_nm_noseeding_broadband
30/03/2020 15:12:47

Counts A	Counts B	Wavelength[nm]	Current[nA]	Power[W]
65.000000	0.000000	500.000000	0.021495	0.011615
81.000000	0.000000	500.000000	0.021199	0.011693
76.000000	0.000000	500.000000	0.020888	0.011585
67.000000	0.000000	500.000000	0.020854	0.011606
87.000000	0.000000	500.000000	0.020376	0.011618
76.000000	0.000000	500.000000	0.020276	0.011886
74.000000	0.000000	500.000000	0.020198	0.011667
66.000000	0.000000	500.000000	0.020384	0.011672
76.000000	0.000000	500.000000	0.020228	0.011582
73.000000	0.000000	500.000000	0.020276	0.011821
71.000000	0.000000	500.000000	0.020342	0.011880
64.000000	0.000000	500.000000	0.020544	0.011906
74.000000	0.000000	500.000000	0.020809	0.011840
67.000000	0.000000	500.000000	0.021070	0.011668
75.000000	0.000000	500.000000	0.020841	0.011499

Figure A2: Fine scan on the As target, no seeding broadband 1 nm step size.

2020-03-27_As_1536_nm_noseeding_broadband
27/03/2020 14:00:15

Counts A	Counts B	Wavelength[nm]	Current[nA]	Power[W]
66.000000	0.000000	500.000000	0.021618	0.013688
71.000000	0.000000	500.000000	0.021655	0.013661
81.000000	0.000000	500.000000	0.021874	0.013548
80.000000	0.000000	500.000000	0.021488	0.013364
94.000000	0.000000	500.000000	0.021576	0.013591
80.000000	0.000000	500.000000	0.021230	0.013563
59.000000	0.000000	500.000000	0.021418	0.013623
78.000000	0.000000	500.000000	0.021677	0.013707
66.000000	0.000000	500.000000	0.021477	0.013521
80.000000	0.000000	500.000000	0.021199	0.013381
71.000000	0.000000	500.000000	0.021224	0.013742
74.000000	0.000000	500.000000	0.021116	0.013518
73.000000	0.000000	500.000000	0.021124	0.012836
70.000000	0.000000	500.000000	0.021386	0.013522

Figure A3: Fine scan on the As target, no seeding broadband 1 nm step size.

Data obtained at GUNILLA for the experiment on the gold target.

```
FineScan-530nm-Au-10per
25/05/2020 11:42:06
Counts A        Counts B        Wavelength[nm]  Current[nA]     Power[W]


5619.000000     18.000000       500.000000      1.417795        0.000729

started measurement at: 25/05/2020 11:42:06

Mean counts A (standard deviation)      5619.000000     NaN

Mean counts B   18.000000       NaN
Disc A  -0.006600

Disc B  -0.006600

Gate A delay    176.300000

Gate B Delay    400.000000

Number of triggers      2000.000000

Number of Periods       40.000000

Notes:  Delay A . 176.3us, width 7us
Delay B. 400us, width 7us
Qswith delay 174.1us, 10% duty cycle, max cur assumed at 80us
```

```
FineScan-531nm-Au-10per
25/05/2020 11:48:54
Counts A        Counts B        Wavelength[nm]  Current[nA]     Power[W]


4134.000000     38.000000       500.000000      1.294822        0.000660

started measurement at: 25/05/2020 11:48:54

Mean counts A (standard deviation)      4134.000000     NaN

Mean counts B   38.000000       NaN
Disc A  -0.006600

Disc B  -0.006600

Gate A delay    176.300000

Gate B Delay    400.000000

Number of triggers      2000.000000

Number of Periods       40.000000

Notes:  Delay A . 176.3us, width 7us
Delay B. 400us, width 7us
Qswith delay 174.1us, 10% duty cycle, max cur assumed at 80us
```

Data obtained for the gold target was subsequently manipulated for computed data analysis.

eV	A	B	Current	Power
2.33932	5619	18	1.417795	0.000729
2.33492	4134	38	1.294822	0.00066
2.33053	3630	38	1.26777	0.000658
2.32616	2330	77	1.227587	0.000531
2.3218	1710	72	1.170377	0.000507
2.31746	1197	72	1.142744	0.000496
2.31314	1002	73	1.133708	0.000446
2.30883	972	75	1.080975	0.000423
2.30454	999	121	1.059991	0.000509
2.30026	982	126	1.045121	0.000493
2.296	940	142	0.99967	0.000504
2.29176	922	127	0.942243	0.000499
2.28753	890	127	0.922061	0.000523
2.28332	924	126	0.906374	0.000502
2.27912	921	144	0.907986	0.000499

Figure A4: Data from scans on the gold target combined into a same file.

energy_1	N_normalized	Scale_N_normalized
2.33932	1	0.067023708
2.33492	0.724960181	0.057160545
2.33053	0.64735438	0.054574584
2.32616	0.338394871	0.036844327
2.3218	0.246386222	0.031748731
2.31746	0.169553043	0.026844411
2.31314	0.126902361	0.022393822
2.30883	0.121881418	0.021983073
2.30454	0.146396421	0.027900691
2.30026	0.140208534	0.027260924
2.296	0.139700226	0.028792399
2.29176	0.1461925	0.029779384
2.28753	0.150275061	0.03140457
2.28332	0.153468592	0.031158839
2.27912	0.148273231	0.031137701

Figure A5: Data from the gold target experiment manipulated to be computed. *N normalized* is the normalization to 1 of the subtracted counts. *Scale N normalized* is the associated error.

The code for the As target written in Matlab:

```
%% Init
clf
clear all
format long

path1 = 'D:\As\As\2020-03-30_As_\';
path2 = 'D:\As\As\2020-03-27_As_\';
filename = "";
data = zeros(32,5);

%Creating the vertical energy lines
x1=[0.8045265924,0.8045265924]; \%the value for x1
x2=[0.8045266202,0.8045266202]; \%the value for x2
yLine=[0.2,1.1]; %y-axis limits  - this is just to create the line between the two dots. I set the
limits to be the same as for the plot size. If you want this line to be longer then you just
change it here

%% load data

WL  = 1535;
for i = 1:16
   filename = strcat(path1,'2020-03-30_As_',num2str(WL)
,'.5_nm_noseeding_broadband.txt');
   dataFile=importfile(filename);
   data(i,1) = WL+.5;
  %data(i,2) = sum(dataFile.Counts_A-dataFile.Counts_B);
   S =
(dataFile.Counts_A-dataFile.Counts_B)./(dataFile.Ion_current.*(1.0*10^(-9)).*dataFile.Laser
_power); %Normalized
   data(i,4) = sum(dataFile.Ion_current.*(1.0*10^(-9)));
   data(i,5) = sum(dataFile.Laser_power);
   data(i,6) = std(dataFile.Counts_A);
   data(i,7) = mean(S);
   data(i,8) = std(S); %main error

   WL = WL + 1;
end

WL  = 1535;
for i = 17:32
   filename = strcat(path2,'2020-03-27_As_',num2str(WL) ,'_nm_noseeding_broadband.txt');
   dataFile=importfile(filename);
   data(i,1) = WL;
   \%data(i,2) = sum(dataFile.Counts_A-dataFile.Counts_B);
```

```
   S =
(dataFile.Counts_A-dataFile.Counts_B)./(dataFile.Ion_current.*(1.0*10^(-9)).*dataFile.Laser
_power); \%Normalized
   data(i,4) = sum(dataFile.Ion_current.*(1.0*10^(-9)));
   data(i,5) = sum(dataFile.Laser_power);
  %data(i,6) = std(dataFile.Counts_A);
   data(i,7) = mean(S);
   data(i,8) = std(S); %main error
   WL = WL + 1;
end



data = sortrows(data,1); %Sorting the data
energy = 1240./data(:,1); %Calculating the energy
ionCurrent=data(:,4); \%Saving the ion current into its own array
laserPower=data(:,5); %Saving the laser power into its own array
signal_AB=data(:,7)/(max(data(:,7)));    \%Saving the data (A-B) into its own array
normalized
error_StDiv=data(:,8)/(max(data(:,7)));
error_x = 5E-5.* ones(32,1);

%% Fit and plot data

% startPoint= [24 750 0.8048];
%startPoint= [0.5 100 0.8048];
[myfit, gof] = createFitAs(energy, signal_AB, error_StDiv);
%fitting = fittype(@(A ,B ,E_0 , x) A + B*sqrt(x - E_0 + abs(x - E_0)));
%myfit = fit(energy, signal_AB, fitting, 'StartPoint', startPoint);
plot(myfit,'k');
hold on
xlim([0.799 0.808])
ylim([0.2 1.1])
plot(x1,yLine, 'g --'); \%Plotting the vertical energy lines x_1 and x_2
plot(x2,yLine, 'c --');
xlabel('Energy [eV]')
ylabel('Norm. counts [a.u.]')
%legend('Data','Fit','Energy x_1','Energy x_2', 'location', 'northwest') \%If you want to include
x_1 and x_2 to the legend use this one and rename the Energy x_1 and Energy x_2 to the
names you want
legend('Data','Fit','location', 'northwest') \%Use this one if you don't want to include x_1 and
x_2 to the legend
```

```
%% EA

CI = confint(myfit, 0.67);

error = max(abs(myfit.E_0-CI(1,3)),abs(myfit.E_0-CI(2,3)));
errorprint=error; \%The EA is 0.80486(3.465741e-05) eV


errorLocString = num2str(abs(floor(log10(error))));

fprintf(strcat('The EA is \%.',errorLocString,'f(\%i) eV\n'), myfit.E_0, errorprint);

fprintf(strcat('\n Done \n'))


end
```

The code for the Au target written in Matlab:

```
clf
clear all
format long

%Creating the vertica energy lines
Scan1_x1=[2.308409737,2.308409737]; %the value for x1
Scan1_x2=[2.308409786,2.308409786]; %the value for x2
Scan1_yLine=[0.2,1.1]; %y-axis limits  - this is just to create the line between the two dots.

% % Import data from text file
[energy_1, N_normalized, Scale_N_normalized] =
importfile('C:\Users\physi\OneDrive\Escritorio\Scans\FineScan1',[2, 16]);

[ev_Au1, CountsA, CountsB, Current_in_A, Power_in_W] =
importfile2('C:\Users\physi\OneDrive\Escritorio\Scans\ErrorFineScan1',[2, 16]);

figure(1)
%plot(energy_Scan1, Signal_norm_Scan1,'bo');
hold on

% % Creating the fit
% % A is the background level
% % B is the amplitude
% % E_0 is the threshold energy
% % x is the freq/energy/wavel
% % sqrt(...) for ^1/2 so for l=0, for p wave ^3/2

countsA_norma=CountsA./(Current_in_A.*Power_in_W);
countsB_norma=CountsB./(Current_in_A.*Power_in_W);

error1_sqrt=sqrt(CountsA+CountsB);
sum_1=(CountsA+CountsB);

error1_sqrt_norma=error1_sqrt./(Current_in_A.*Power_in_W);
errorscale1=error1_sqrt_norma;

errorbar(energy_1, N_normalized, Scale_N_normalized,'.r','MarkerSize',6,...
   'MarkerEdgeColor','black','MarkerFaceColor','black')
hold on

startPoint1= [0.31 100 2.3086];

[myfit2, gof] = createFit2(energy_1, N_normalized, Scale_N_normalized);

figure(1)
plot(myfit2,'k');
```

```
hold on

xlim([2.27 2.34])
ylim([0.2 1.1])
plot(Scan1_x1,Scan1_yLine, 'g --'); %Plotting the vertical energy lines x_1 and x_2
plot(Scan1_x2,Scan1_yLine, 'c --');
xlabel('Energy [eV]')
ylabel('Norm. counts [a.u.]')
%legend('Data','Fit','Energy x_1','Energy x_2', 'location', 'northwest') %Rename Energy x_1
and Energy x_2 to the names you want
legend('Data','Fit','location', 'northwest') %Use this one if you don't want to include the x_1
and x_2 to the legend


% % % %EA for scan1
CI1 = confint(myfit2, 0.67);
error1_sqrt = max(abs(myfit2.E_0-CI1(1,3)),abs(myfit2.E_0-CI1(2,3)));
errorprint1=error1_sqrt;

%fprintf('The uncertainty is %.', myfit2.E_0, errorprint1);
 errorLocString1 = num2str(abs(floor(log10(error1_sqrt)))); %Converting a number into a
character
 fprintf(strcat('The EA for scan1 is %.',errorLocString1,'f(%i) eV\n'), myfit2.E_0, errorprint1);
%Writing out the EA (myfit4.E_0) and its error (errorprint)
```

Bibliography

[1] J. Navarrete. Master Thesis. An Experimental Determination of the Electron Affinity of Cesium. *Univerity of Gothenburg*, pages 7-13, 2019.

[2] J.Welander. Thesis For The Degree of Licenciate. The Negative Nature of Elements. *University of Gothenburg*, pages 1-8, 17-27, 2019.

[3] J.J. Thomson. Bakerian Lecture: Rays of positive electricity. *Proceedings of the Royal Society of London A: Mathematical, Physical and Engineering Sciences*, **89**:pages 1-15, 1913.

[4] R. Wildth. Negative ions of hydrogen and the opacity of stellar atmospheres. *The Astrophysical Journal*, **90**:pages 612-613, 1939.

[5] A. Ringwall-Moberg. Master Thesis. Photodetachment Studies of Negative Ions of Iodine. *University of Gothenburg*, pages 1-7, 2016.

[6] E.P. Wigner. On the Behavior of Cross Sections Near Thresholds. *Phys. Rev.*, **73**:pages 1002-1009, 1948.

[7] D. Hanstorp and D.J. Pegg. Photodetachment. *Springer Handbook of Atomic, Molecular and Optical Physics*, (Chapter 60. 2nd Ed.):pages 1-32, 2020.

[8] C.L. Bennett. Radiocarbon Dating Using Electrostatic Accelerators: Negative Ions Provide the Key. *Science Magazine*, **198**:pages 508-510, 1977.

[9] Detector technology, inc. http://www.detechinc.com/technotes.html, 2020.

[10] B. Brehm, M.A. Gusinow, and J.L. Hall. Electron Affinity of Helium via Laser Photodetachment of its Negative Ion. *Phys. Rev. Letters*, **19**:pages 737-741, 1967.

[11] M.J. Weber. Handbook of Laser Wavelengths. *CRC Press*, page 30, 1999.

[12] T. Andersen, H.K. Haugen, and H. Hotop. Binding Energies in Atomic Negative Ions: III. *J. Phys. Chem*, **28**:pages 1527-1528, 1999.

[13] C. Diehl, K. Wendt, A. O. Lindahl, P. Andersson, and D. Hanstorp. Ion Optical Design of a Collinear Laser-negative Ion Beam Apparatus. *Review of Scientific Instruments*, **82**:p. 053302., 2011.

[14] WHO. Arsenic. https://www.who.int/news-room/fact-sheets/detail/arsenic, 2021.

[15] M. Génévriez, A. Dochain X. Urbain, A. Hibbert, R. Marion, K.M. Dunseath, and M. Terao-Dunseath. One and Two Photodetachments of O^- *Physical Review*, A**98**:pages 0334101, 2018.

[16] N. Bohr. On the Constitution of Atoms and Molecules. *Philosophical Magazine*, **6**:pages 857-875, 1913.

[17] L. De Broglie. Recherches sur la Theorie des Quanta. *Annales de Physique*, **10**:pages 22-128, 1913.

[18] W. Heisenberg. On the Descriptive Content of Quantum Theoretical Kinematics and Mechanics. *Z.Physik*, **43**:pages 172-198, 1927.

[19] J. Rohlen. Thesis For The Degree of Doctor in Philosophy. Excited States in Negative Ions. *University of Gothenburg*, page 7, 2014.

[20] P. Andersson. Thesis For The Degree of Doctor of Philosophy. Laser Photodetachment of Negative Ions, Fundamental Research and Applications. *Department of Physics, University of Gothenburg*, pages 5-11, 33, April 2009.

[21] J. Warbinek. Master Thesis. Spectroscopy of Negative Ions. *University of Gothenburg-University of Mainz*, pages 27, 51-53, 2020.

[22] C. W. Walter, N.D. Gibson, R.L. Field III, A.P. Snedden, J.Z. Shapiro, C.M. Janczak, and D. Hanstorp. Electron Affinity of Arsenic and the Fine Structure of As^- Measured Using Infrared Photodetachment Threshold Spectroscopy. *Physical Review*, A**80**:pages 0145011, 2009.

[23] L. A. A. Nikolopoulos. Calculation Method for the Continuum States of Atomic Systems. *Central European Journal of Physics*, **11**:page 1074, 2013.

[24] H. Friedrich. *Theoretical Atomic Physics*. Springer, 3era edition, 2006.

[25] D. J. Griffiths. *Introduction to Quantum Mechanics (2nd Edition)*. Pearson Prentice Hall, 2nd edition, April 2004.

[26] H. Hotop and W.C. Lineberger. Dye-laser Photodetachment Studies of Au^- Pt^- PtN^- and Ag^- *The Journal of Chemical Physics*, **58**:pages 2381-2385, 1972.

[27] H. Hotop, R.A. Bennett, and W.C. Lineberger. Electron affinities of Cu and Ag. *The Journal Chemical Physics*, **58**:pages 2374-2375, August 1973.

[28] I.A. Álvarez Guzmán. Laser Photodetachment Threshold Spectroscopy of ^{127}I by Doppler Tuning. *Master Thesis, University of Gothenburg*, pages 20, 21, 2016.

[29] V.E. Khrohn. Emission of Negative Ions from Metal Surfaces Bombarded by Positive Cesium Ions. *Journal of Applied Physics*, **33**:pages 3523-3525, 1962.

[30] R. Middleton. A Negative-Ion Cookbook. *University of Pennsylvania Press*, pages 88-89, 115-116, 180, 1989.

[31] R.P. Feynman, R. B. Leighton, and M. Sands. *The Feynman Lectures on Physics; New millennium ed.* Basic Books, New York, NY, 2010. Originally published 1963-1965.

[32] HRL Laboratories. The First Laser. https://www.hrl.com/about/laser, 2020.

[33] Spectra Physics. Quanta-Ray MOPO-HF, Optical Parametric Oscillator. User's Manual. pages 1-15, 2002.

[34] Photonics Encyclopedia. Titanium-Sapphire lasers. https://www.rp-photonics.com/titanium_sapphire_lasers.html, 2021.

[35] Photonics Encyclopedia. Diode lasers. https://www.rpphotonics.com/diode_lasers.html, 2020.

[36] EGISMOS. Opto. Electronics. Laser Diodes: IR, Red, Green, Blue laser diode. http://www.egismos.com/laser-diode.html, 2020.

[37] Peabody Scientific. Negative Ion Sputter Source. http://www.peabody-scientific.com/page13.html, 2021.

[38] Behlke High tech in high voltage. Fast High Voltage Solid State Switches. http://www.hv-switch.com/, 2021.

[39] M. Bodendorfer, K. Altwegg, H. Shea, and P. Wurz. Field Structure and Electron Life Times in the Mefisto Electron Cyclotoron Resonance Ion Source. *Plasma Physics*, **266**:pages 1,2, 2008.

[40] F. Brouillard and P. Defrance. Animated Crossed Beams for the Measurement of Electron Impact Ionisation. *Physica Scripta.* T**3**:pages 68-70, 1983.

[41] M.Génévriez and X.Urbain. Animated-Beam Measurement of the Photodetachment Cross Section of H^- *Physical Review*, **91**:033403, 2015.

[42] T. Nzeyimana. Etude Expérimentale de l'association Ionisante Entre l'ion O^- et Divers Ions Positifs (D^+, C^+, N^+, O^+, $H_2{}^+$, CO^+ et $N_2{}^+$). *Degree Doctorat en Sciences (Sciences Physiques), Université Catholique de Louvain-la-Neuve*, pages 27-37, 2003.

[43] CEM Models / Standard CEMs. Characteristics of standard CEMs. http://www.sjuts.com/CEMModels_Standard.html, 2021.

[44] COHERENT. Verdi V Series. https://www.coherent.com/lasers/laser/verdi-vseries, 2020.

[45] CNL. Violet Diode Laser at 405 nm. http://www.cnilaser.com/PDF/MDL-III-405.pdf, 2020.

[46] M.Y. Amusia, G. F. GribakinS, V. K. Ivanovz and L. V. Chernyshevas. Many-electron Correlations in Negative-ion Photodetachment. *Journal of Physics B: Atomic, Molecular and Optical Physics.* **23**:pages 385-391, 1990.